



## OPEN New insights into structural, optical, electrical and thermoelectric behavior of $\text{Na}_{0.5}\text{Bi}_{0.5}\text{TiO}_3$ single crystals

G. Jagło<sup>1✉</sup>, Kamila Kluczevska-Chmielarz<sup>1✉</sup>, J. Suchanicz<sup>2</sup>, A. Kruk<sup>1</sup>, A. Kania<sup>3</sup>, D. Sitko<sup>4</sup>, M. Nowakowska-Malczyk<sup>4</sup>, M. Łapiński<sup>5</sup> & G. Stachowski<sup>6</sup>

The single crystals of lead-free  $\text{Na}_{0.5}\text{Bi}_{0.5}\text{TiO}_3$  were grown using the Czochralski method. The energy gaps determined from X-ray photoelectron spectroscopy (XPS) and optical measurements were approximately 2.92 eV. The current-voltage characteristics, depolarization current, dc ( $\sigma_{dc}$ ) and ac ( $\sigma_{ac}$ ) electrical conductivity, and Seebeck coefficient of the crystals were investigated. The frequency/temperature-dependent electrical properties were also measured and analyzed through complex impedance spectroscopy. An overlapping reversible insulator-metal transition (resistive switching) on nanoscales, caused by the electric field, was detected. Most of these properties were measured for the first time. The activation energy values determined from the conductivity data, the imaginary part of the electric impedance and the modulus indicate that the relaxation process in the high-temperature range is attributable to both single and double ionized oxygen vacancies, in combination with the hopping of electrons between  $\text{Ti}^{4+}$  and  $\text{Ti}^{3+}$ . P-type electrical conductivity was also found. These discoveries create new possibilities of reducing the electrical conductivity of NBT and improving the process of effectively poling this material. Our results indicate the possibility of tuning the material properties by intentionally creating non-stoichiometry/structural defects (oxygen vacancies, cation excess and cation deficiency).

**Keywords**  $\text{Na}_{0.5}\text{Bi}_{0.5}\text{TiO}_3$  single crystals, Insulator-metal transition, Electrical conductivities, Relaxation process.

Lead-based materials, such as PZT, PMN, PFN, etc., have been widely used due to their excellent electromechanical properties<sup>1–4</sup>. However, the high toxicity and high volatility of lead oxide (PbO) results in environmental pollution, generates compositional inhomogeneities and the formation of an undesirable pyrochlore phase. For these reasons, it is strongly recommended that non-toxic materials are developed for use in various devices such as transducers, actuators, filters, multilayer capacitors, etc.<sup>1,5</sup>. One such important material is sodium-bismuth titanate,  $\text{Na}_{0.5}\text{Bi}_{0.5}\text{TiO}_3$  (NBT).

NBT has a perovskite ( $\text{ABO}_3$ ) structure with rhombohedral symmetry (R3c) with ion displacements along the [111] direction of the pseudocubic cell and with out-of-phase  $\bar{a}\bar{a}\bar{a}$ .

octahedral tilting at room temperature, however monoclinic or rhombohedral/monoclinic mixtures have been also postulated<sup>6,7</sup>. NBT exhibits ferroelectric properties with remnant polarization  $P_r=20\text{--}35\ \mu\text{C}/\text{cm}^2$  and coercive field  $E_c\approx 70\text{--}90\ \text{kV}/\text{cm}$  at room temperature. On heating, it undergoes the following sequence of diffused structural transformations: rhombohedral (R3c)  $\rightarrow$  tetragonal (P4bm) at  $T_{R-T}=260\text{--}400\ \text{°C}$   $\rightarrow$  cubic (Pm3m) at  $T_{T-C}=520\text{--}540\ \text{°C}$ . The tetragonal phase is non-polar or weakly polar. The results of transmission electron microscopy (TEM) studies<sup>8,9</sup> suggest that the rhombohedral-tetragonal phase transformation occurs

<sup>1</sup>Institute of Technical Sciences, University of the National Education Commission, Podchorążych 2, Krakow 30-084, Poland. <sup>2</sup>Department of Mechanical Engineering and Agrophysics, University of Agriculture in Krakow, Balicka 120, Krakow 31-120, Poland. <sup>3</sup>A.Chelkowski Institute of Physics, University of Silesia in Katowice, 75 Pułku Piechoty, Chorzów 41-500, Poland. <sup>4</sup>Faculty of Exact & Natural Sciences, University of the National Education Commission, ul., Podchorążych 2, Krakow 30-084, Poland. <sup>5</sup>Institute of Nanotechnology and Materials Engineering, Advanced Materials Center, Gdansk University of Technology, Gdańsk 80-233, Poland. <sup>6</sup>Astronomical Observatory, Jagiellonian University, Orla 171, Krakow 30-244, Poland. ✉email: grzegorz.jaglo@uken.krakow.pl; kamila.kluczevska-chmielarz@uken.krakow.pl

in two steps: the disintegration of the rhombohedral R3c domains via a microtwinning process starts at the so-called “depolarization temperature”  $T_d \approx 170\text{--}190^\circ\text{C}$ , and the rhombohedral-tetragonal phase transition at approximately  $279^\circ\text{C}$  may proceed through the intermediate modulated orthorhombic Pnma phase<sup>8</sup>. The twin boundaries between ferroelectric rhombohedral micro-domains form the sheets of this intermediate phase. However, the existence of the orthorhombic phase has not been fully confirmed<sup>10</sup>.

At  $T_d$ , NBT loses its long-range ferroelectric state and transforms into a short-range relaxor-like state<sup>5</sup>. In the vicinity of  $T_d$ , dielectric dispersion increases and a frequency dependent bump exists in the temperature evolution of electric permittivity  $\epsilon(T)$ . A broad maximum of electric permittivity is observed at  $T_m \approx 320^\circ\text{C}$ , which does not correspond to any structural transformation and may instead originate from a dielectric relaxation attributed to an electromechanical interaction between polar regions and the non-polar matrix<sup>11</sup>. The existence of polar regions far above  $T_m$  was proved by Vakhrushev et al.<sup>12</sup> and confirmed by Suchanicz et al.<sup>11,13,14</sup>. These regions become the nuclei of the emerging ferroelectric phase.

Despite numerous studies to date, contradictory conclusions on the number, sequence and type of the electric order of the particular phases in NBT can be found in the literature and opposing opinions have been presented by various researchers. Particularly, the phase properties in the temperature interval  $200\text{--}350^\circ\text{C}$  have been the subject of some controversy, as either having a mixture of tetragonal and rhombohedral phases with polar regions<sup>11</sup> or being antiferroelectric<sup>15</sup>. Deviations from the average rhombohedral structure<sup>16</sup> and incommensurate<sup>17</sup> phase have been also postulated. Some of these discrepancies can be attributed to structural imperfections, arising from the impurity of the initial components and different technologies or sintering conditions of the ceramic and crystal. The too high electrical conductivity of NBT causes difficulties in poling it effectively. Therefore, understanding of the mechanisms behind the appearance this high conductivity is a priority.

As mentioned above, the available information concerning the properties of NBT is still incomplete and inconsistent. Most experimental results for NBT were obtained using ceramic samples, however, single crystals usually offer better properties than those of polycrystalline ceramics. The pore-free microstructure of single crystals positively influences the operating life of devices, since pores and other microstructural imperfections are usually responsible for material failures. Besides, the issues of grain size and porosity can be ignored for single crystals, which makes for easier, and more certain, interpretation of experimental data. However, the growth of high-quality and large-size  $\text{Na}_{0.5}\text{Bi}_{0.5}\text{TiO}_3$  single crystals continues to be a challenge.

The knowledge of the electronic structure of a material is key to understanding and modifying its physical and chemical behavior. X-ray photoelectron spectroscopy (XPS) is a powerful method to study the electronic structure of matter. As electrical transport behavior influences other associated properties such as dielectric losses, pyroelectricity, piezoelectricity, and also the strategy used for poling, the study of these behavior is extremely important. Moreover, these kinds of studies, particularly of NBT single crystals, are rare in the existing literature<sup>18–21</sup>. To our knowledge, there are no prior results on the depolarization current, current-voltage (I-U) characteristics, Seebeck coefficient and thermal conductivity for NBT single crystals.

In the present paper we report the results of XPS, X-ray, depolarization current, I-U characteristics, Seebeck coefficient, dc/ac electrical conductivity and thermal conductivity studies of  $\text{Na}_{0.5}\text{Bi}_{0.5}\text{TiO}_3$  single crystals grown by the Czochralski method. To clarify the electrical conductivity phenomenon, the Electrochemical Impedance Spectroscopy (EIS) method was used.

## Experimental procedures

$\text{Na}_{0.5}\text{Bi}_{0.5}\text{TiO}_3$  single crystals were grown by the Czochralski method. Powder reagents  $\text{NaHCO}_3$  (99.7%),  $\text{Bi}_2\text{O}_3$  (99.9%) and  $\text{TiO}_2$  (99.9%) were weighed in stoichiometric ratio and homogenized in an agate mortar for 24 h with ethanol. Using non-hygroscopic  $\text{NaHCO}_3$  instead of hygroscopic  $\text{Na}_2\text{CO}_3$  allowed for careful adjustment of the stoichiometry during weighing. In addition, to eliminate carbonate decomposition of  $\text{Bi}_2\text{O}_3$ , it was thermally treated at  $400^\circ\text{C}$  for 9 h. Both treatments were intended to minimize the effect of uncertainties in the stoichiometry of the samples. The milled powders were then dried, calcined at  $800^\circ\text{C}$  for 2 h and at  $950^\circ\text{C}$  for 5 h. The calcined material was placed in a Pt crucible, heated to  $1300^\circ\text{C}$  and then soaked for 2.5 h. The crystal growth was carried out at  $1300^\circ\text{C}$  in air. The crystal was pulled and rotated at rates of 5 mm/h and 20 rpm, respectively. Slightly yellowish, transparent cub-shaped single crystals of 1.5 cm in size and piezoelectric coefficients  $d_{33} = 91\text{pC/N}$  and  $k_{33} = 34\%$  were obtained.

The XRD investigations were performed using a Philips X'Pert Pro MD diffractometer. Standard Bragg-Brentano geometry was applied with  $\text{CuK}_{\alpha 1,2}$  radiation (the  $\text{K}_{\beta}$  line was suppressed by a Ni filter). All measurements were performed in air in the  $2\theta$  scanning range  $20^\circ\text{--}100^\circ$  with a step of  $0.017^\circ$ .

X-ray photoelectron spectroscopy (XPS) was used to determine the precise chemical compositions and oxidation states of the elements on the sample surface. The XPS measurements were performed using Omicron Nano-Science equipment with a hemispherical 128-channel Argus spectrometer. Experiments were conducted at room temperature under ultra-high vacuum conditions at pressure below  $1.1 \times 10^{-6}$  Pa. The obtained spectra were analysed by the CASA XPS software package, using Shirley background subtraction and the Gauss-Lorentz curve, GL (30), fitting algorithm through the least-squares method. To calibrate the results, a binding energy of  $285.00\text{ eV}$  was established as the reference energy for the C1s signal (peak).

The dimensions of the samples were  $4 \times 4 \times 0.3\text{ mm}$  with two main faces perpendicular to the  $[001]_c$  direction. The  $[001]_c$  faces of the samples were optically polished and coated with silver electrodes. The samples were annealed at a temperature above the tetragonal-cubic phase transition for 1 h.

The direct electric conductivity ( $\sigma_{dc}$ ) was measured over a temperature range from room temperature to  $600^\circ\text{C}$  using a Keithley 6517 A electrometer. The alternating current electric conductivity ( $\sigma_{ac}$ ) and impedance spectroscopy were measured in a frequency/temperature range  $100\text{ Hz--}2\text{ MHz}$  and from room temperature to  $600^\circ\text{C}$  for silver electrode samples using a GW 821LCR meter.

The depolarization currents and current-voltages ( $I$ - $U$ ) characteristics were measured using a Keithley 6517 A electrometer. As these measurements require precise temperature stabilization to avoid the influence of pyrocurrents, stabilization within 0.1 °C was maintained. In case of depolarization currents measurements, the sample was polarized at 5, 15 and 25 kV/cm for 1–2 h at the chosen temperature. Next it was short-circuited and the depolarization current flowing from the sample was measured.

The Seebeck coefficient ( $\alpha$ ) was measured in the temperature range 50–370 °C. The sample was placed in a thermostat between heated silver blocks, which made it possible to create a temperature gradient inside the sample (for more details see<sup>22</sup>). The temperature difference between the electrodes of the sample  $\Delta T$  was varied from 0 to 10 °C at each chosen temperature. Values of the Seebeck coefficient were determined from the slope of the linear dependencies of the electromotive force  $E$  vs. the temperature difference  $\Delta T$ .

## Results and discussion

### X-ray results

Figure 1a shows the photo of the as-grown NBT single crystal. It is slightly yellowish, transparent and no obvious cracks are observed. The room-temperature X-ray pattern of NBT single crystals are shown in Fig. 1b. X-ray spectrum does not contain reflections related to the second phases which points to the high quality of the studied crystals. The well-defined splitting of the  $(110)_c$  and  $(111)_c$  reflections, a small superreflection near 38° (indicated by an arrow) and the complex character of the  $(200)_c$  reflections reveal rhombohedral ( $R3c$ ) symmetry with a small content of tetragonal phase.

Figure 2 plots the central  $2\Theta$ -positions of the structure sensitive  $(110)_c$ ,  $(111)_c$  and  $(200)_c$  Bragg reflections (peaks) against temperature. It can be seen that a constant lower-angle shift exists and some anomalies of the  $2\Theta(T)$  curves at about 260 °C (for  $(110)_c$ ,  $(111)_c$  and  $(200)_c$  peaks) and at about 350 and 520 °C (for  $(200)_c$  peak) are visible (indicated by arrows). The lower-angle shift of the peaks indicates a gradual increase of unit cell volume with rising temperature. The first and last anomalies are attributed, respectively to the transformations from rhombohedral to tetragonal phase, and from tetragonal to cubic phase. However, the second anomaly corresponds with  $T_m$  and reflects the dominance of the tetragonal phase in the range of coexistence of the rhombohedral and tetragonal phases. The phase transformation between the rhombohedral and tetragonal phases takes place successively in a wide range of temperatures, hence two anomalies are visible, the first one around 260 °C, where the highest rate of growth of the tetragonal phase occurs at the expense of the rhombohedral phase, and the second one around 350 °C, where the dominant phase is already the tetragonal phase.

### XPS results

The XPS measurements of NBT single crystals were performed to analyse their chemical composition and the valence states of the particular elements. Figure 3a shows the survey spectrum. The average chemical composition calculated using the XPS spectra was estimated to be  $\text{Na}_{0.53}\text{Bi}_{0.65}\text{TiO}_{2.8}$  and it is approximately close to the nominal composition. There is an excess of sodium and bismuth and a deficiency of oxygen. These results confirm the crystal composition obtained from the EDS spectra. Additionally, carbon was detected, due to absorption from the atmosphere. In Fig. 3b-d the high-resolution spectra for Na1s, Bi4f and Ti2p regions are presented. The signal recorded for Na1s is characteristic of the  $\text{Na}^+$  state<sup>23,24</sup>, while the characteristic doublet visible in Fig. 3c could be assigned to  $\text{Bi}^{3+}$ <sup>25,26</sup>. The spectrum recorded for the Ti2p region is more complicated due to overlapping of the Ti2p doublet and Bi4d singlet<sup>27</sup>. The curve was deconvoluted into three peaks, corresponding to  $\text{Bi}4d_{3/2}$ ,  $\text{Ti}2p_{1/2}$  and  $\text{Ti}2p_{3/2}$ . The positions of the peaks and the splitting energy, equal to 5.7 eV, is characteristic of the  $\text{Ti}^{4+}$  state<sup>28</sup>.

### Optical results

Figure 4a shown absorption coefficient spectra for NBT crystals. As can be seen, the examined materials are translucent in the visible and near infrared range. As the wavelength increases, a significant decrease in the

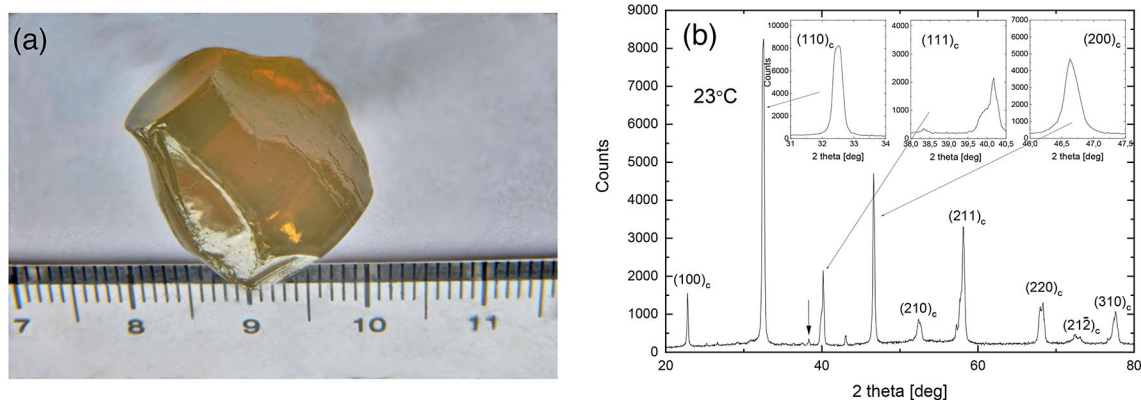


**Fig. 1.** The photo of the as-grown NBT crystal (a) and room-temperature X-ray pattern (b) of NBT single crystals.

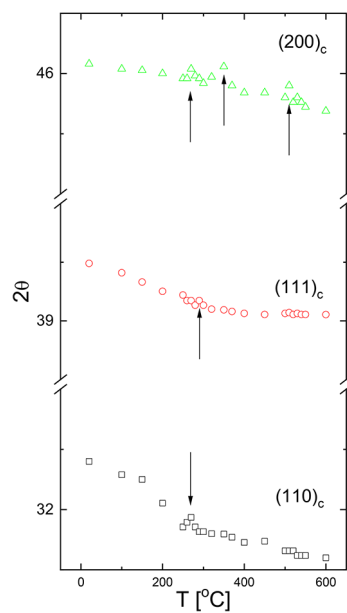


**Fig. 2.** The temperature dependence of the central  $2\theta$ -positions of the  $(110)_c$ ,  $(111)_c$  and  $(200)_c$  Bragg reflections.

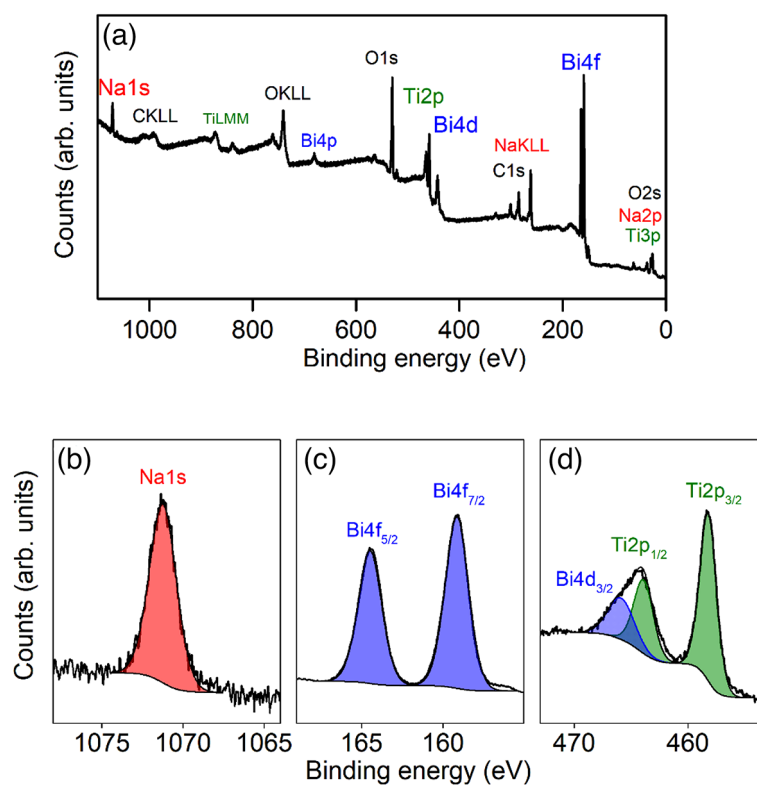


**Fig. 3.** XPS overview spectrum (a) and high-resolution Na1s (b), Bi4f (c), Bi4d and Ti2p (d) core level spectra of NBT single crystals.

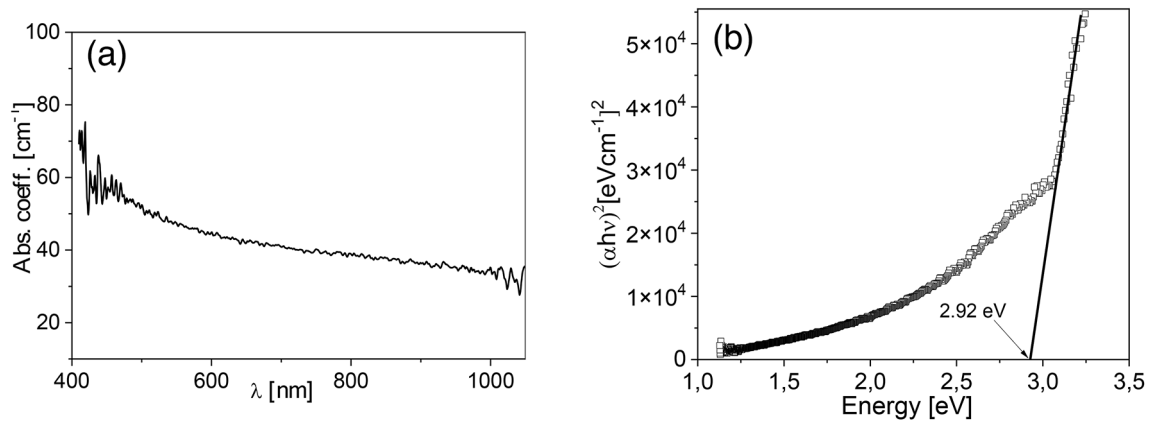


**Fig. 4.** Absorption coefficient spectra (a) and Tauc's plot (b) for NBT single crystals.

material's absorption coefficient is observed, which is consistent with the theory of light scattering on defects<sup>29</sup>. The absorption spectrum was fitted to the dependence expressed by<sup>30</sup>:

$$\alpha = \frac{(hv - E_g)^{1/n}}{hv} \quad (1)$$

where  $\alpha$  denotes the linear absorption coefficient of the material,  $hv$  denotes the photon energy,  $E_g$  denotes the band gap energy. The value of  $n$  is  $\frac{1}{2}$  for direct allowed transitions and equal to 2 for indirect allowed transitions. Extrapolation of a straight-line plot of  $\alpha hv$  vs.  $hv$  intercepts the horizontal axis giving the value of  $E_g$  (Fig. 4b). The best fit indicates that NBT has a direct band gap ( $n=\frac{1}{2}$ ) of approximately  $2.92 \pm 0.02$  eV. This energy corresponds to a wavelength of approximately 400 nm, below which the incident light is completely absorbed. Literature data indicate a slightly higher energy gap from 3 to 3.2 eV for NBT single crystals<sup>31,32</sup> and doped ones<sup>33</sup>, as well as for the epitaxial layer<sup>34</sup>.

### Current–voltage characteristics

Figure 5 presents the set of current-voltage  $I(U)$  characteristics for the NBT single crystals. For the longest duration of the applied electric field, we are dealing with so-called saturation. Analysis of the  $I(U)$  characteristics showed that the classical Ohm's law was obeyed at low values of the applied electric field, and the range of its applicability strongly depends on the measurement duration. Linear fragments can be distinguished in  $I(U)$  curves with different slopes, satisfying the relationship<sup>21</sup>:

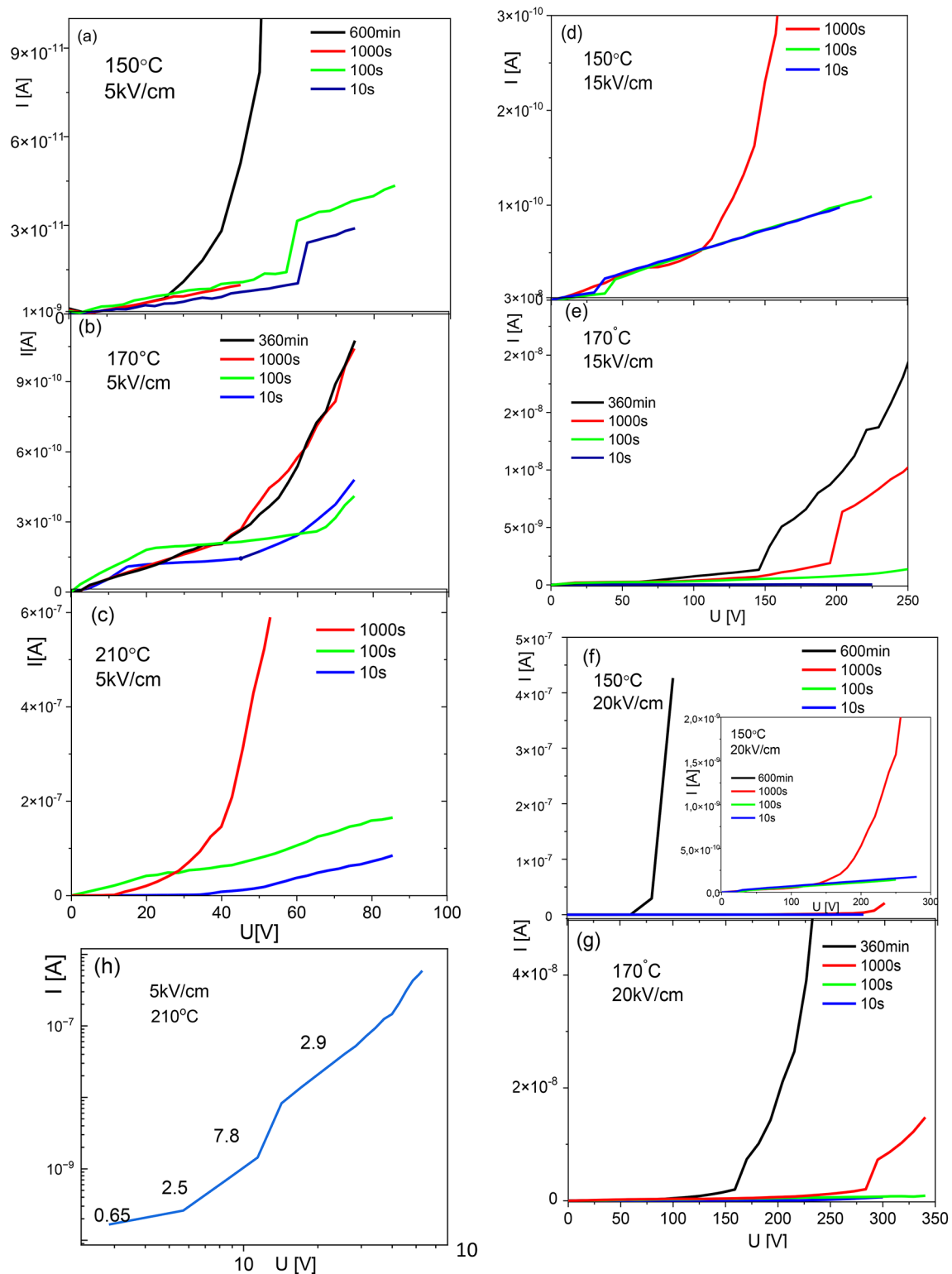
$$I \sim U^n \quad (2)$$

Figure 5h shows as a “double” logarithmic (log-log) plot of the  $I(U)$  relationship at 210 °C. The  $I(U)$  curve shows the adjustment values of the  $n$  parameter measured at a given voltage of 5 kV/cm. As can be seen, approximate agreement with Ohm's law has been ascertained at low electric field strength. When certain voltage limits are exceeded, the  $I(U)$  angle increases, which suggests a decrease in resistance and a change in the conduction mechanism. At higher temperatures and voltages, the material begins to exhibit semiconductor properties, which is related to the thermal activation of electric charge carriers and easier injection of carriers into the material. Further increasing the temperature and voltage leads to conduction, which agrees with the *space-charge-limited current (SCLC)* theory<sup>35</sup>. According to this theory, material defects are a source of trap states in which trapped charge carriers are excited only by a high external electric field and thermal energy. The concentration of excess injected charges at high electric field is greater than that of thermal equilibrium charges. As the temperature increases, the concentration of equilibrium charges (holes and electrons) increases, which may lead to the appearance of *SCLC* space charge towards higher electric fields, which is confirmed by the results presented in Fig. 5. When the electric field reaches the *trap-filled limited (TFL)*, the electric current increases faster and the  $I(U)$  characteristics depend on the trap distribution according to the relationship  $I \sim U^m$  ( $m = 2, 4$ ).

In order to determine the transition point between behavior consistent with Ohm's law and the *SCLC* rule, the voltage value is introduced, as defined by the formula<sup>21,36</sup>:

$$V_{SCLS} = \frac{ed^2n}{2\epsilon\epsilon_0\theta} \quad (3)$$

where  $e$  – electron charge,  $d$  – sample thickness,  $n$  – thermal equilibrium of the density of free carriers,  $\epsilon$  – electrical permittivity of the material,  $\epsilon_0$  – vacuum electrical permittivity, and  $\theta$  – a coefficient determining the degree of charge trapping, given by the formula:



**Fig. 5.** Current-voltage characteristics (a–g) and double logarithmic relationship  $I(U)$  (h) for the NBT single crystals. Insert in (f) shows an expanded part of this Figure. The numbers above the  $I(U)$  graph in (h) indicate the values of the exponent  $n$  from the formula  $I \sim U^n$ . (i) shows an example of the network of dark stripes on the sample.

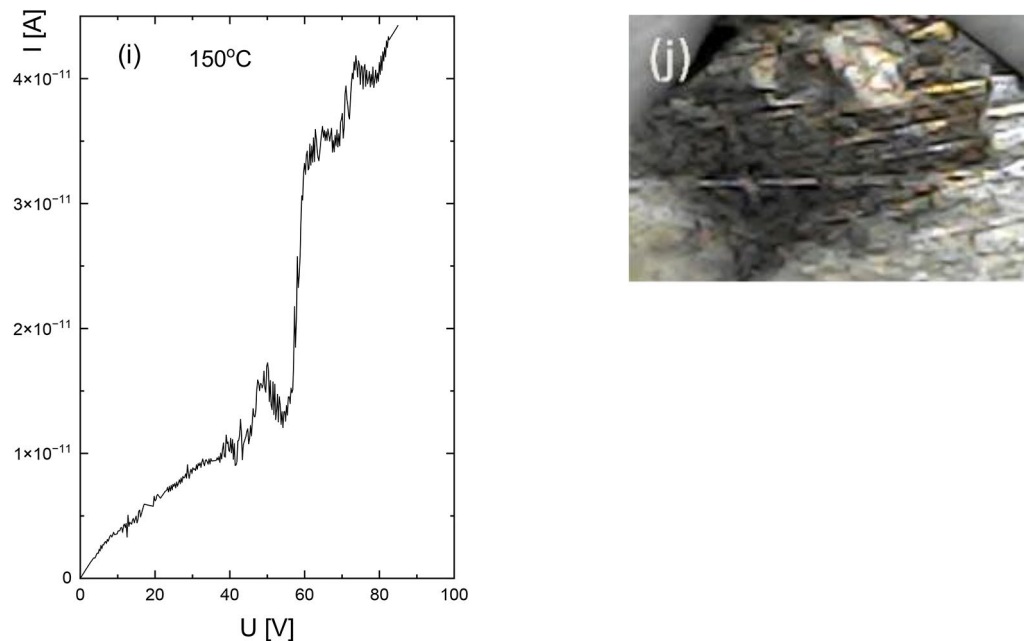


**Figure 5.** (continued)

$$\theta = \frac{n}{n_t} = \frac{N_c}{gN_t} \exp\left(\frac{E_t - E_c}{k_B T}\right) = \frac{N_c}{gN_t} \exp\left(\frac{-E_t}{k_B T}\right) \quad (4)$$

where  $n_t$  – density of trapped charges,  $N_c$  – density of states in the conduction band,  $N_t$  – trap density,  $g=2$  – degradation coefficient,  $E_t$  – trap energy below the edge of the conduction band  $E_c$ . From relation (3) we get:

$$\theta = \frac{d^2 \sigma}{2\epsilon \epsilon_0 \mu V_{SCLC}} \quad (5)$$

where:  $e$  – electron charge ( $1.602 \times 10^{-19}$  C),  $d$  – sample thickness ( $0.0005$  m),  $\epsilon = 3746$ ,  $\epsilon_0 =$

$8.85 \times 10^{-12}$  F/m,  $\mu = 10^{-10}$  m<sup>2</sup>/Vs,  $V_{SCLC} = 60$  V. The  $\theta$  coefficient determined from the above equation is  $1.97 \times 10^{-2}$  for a temperature of  $150^\circ\text{C}$  (below  $T_d$ ). The estimated value is consistent with literature data for materials with a perovskite structure<sup>21,37</sup>.

Based on the experimental data, the density of traps  $N_t$  and the trap-filled limited voltage  $V_{TFL}$  was calculated for selected temperatures of  $150$ ,  $170$  and  $210^\circ\text{C}$ . The obtained values are summarized in Table 1. As the value of the applied electric field increases, the value of the  $V_{TFL}$  voltage, at which the traps are filled decreases. At a temperature of  $170^\circ\text{C}$ , a significant increase in the  $V_{TFL}$  voltage is observed, resulting from the presence of the depolarization phenomenon. At  $210^\circ\text{C}$ , i.e. above the depolarization temperature, the same  $V_{TFL}$  value is recorded as at  $150^\circ\text{C}$ , but for a much higher field  $E = 20$  kV/cm. Based on the analysis of these relationships, the presence of shallow traps in the material is confirmed<sup>21,37</sup>.

Another explanation of the current-voltage characteristics is presented in paper<sup>38</sup>, i.e. an overlapping reversible insulator-metal transition (resistive switching) on nanoscales caused by the electric field. As a result of non-stoichiometry, both point and extension defects (shear planes) may appear in perovskites. In our NBT single crystals non-stoichiometry exists (see XPS results). In particular, a deficiency of oxygen is observed. As shown in paper<sup>38</sup>, a tendency toward vacancy clustering is observed. This ordering dominates in the temperature range below the Tamman temperature, which is about half of the melting temperature (about  $600^\circ\text{C}$  for NBT

T [°C]	E [kV/cm]	V <sub>TFL</sub> [V]	N <sub>t</sub> [1/m <sup>3</sup> ]
150	5	60	$8.7 \cdot 10^{20}$
150	15	40	$5.8 \cdot 10^{20}$
150	20	30	$4.4 \cdot 10^{20}$
170	15	210	$3.0 \cdot 10^{21}$
170	20	270	$3.9 \cdot 10^{21}$
210	5	30	$4.4 \cdot 10^{20}$

**Table 1.** The value of the electric field  $E$ , the limiting voltage of filling the traps  $V_{TFL}$  and the volume density of the traps  $N_t$  at selected temperatures.

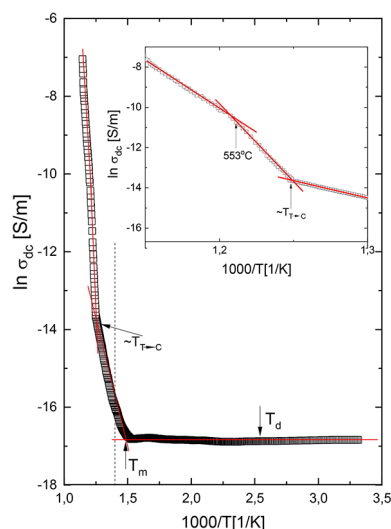


**Fig. 6.** Direct current conductivity  $\sigma_{dc}$  vs.  $1000/T$  measured using 4-electrode method of NBT single crystals. Vertical dotted line indicates  $T = 400^\circ\text{C}$ . Insert shows expanded part of this Figure.

Temperature range [ $^\circ\text{C}$ ]	Activation energy $E_a$ [eV]
100–195	0.03
200–350	0.43
350–450	1.26
450–550	1.18
553–600	1.14

**Table 2.** Activation energy for NBT single crystals obtained from DC conductivity data in various temperature ranges.

single crystals), including the temperature range over which the current-voltage characteristics were measured in the present paper. For low concentration of vacancies, the oxygen defects can be ordered along columns with different lengths of each segment and the segments (further called filaments) can be statistically distributed in the matrix<sup>38</sup>. Increasing oxygen nonstoichiometry leads to a rapid increase of the number of these filaments and introduces an additional parallel orientation between them lying close to each other. In consequence, oxygen defects are not randomly distributed but tend to be arranged in regular patterns. Conduction of the filaments relative to the matrix is 4–5 orders of magnitude higher<sup>38</sup>. It was concluded, that reduction of the Ti valence as an effect of an enhanced local oxygen deficiency along the Ti-rich core of the edge shear planes (dislocations) causes an increase of the conductivity along the dislocations core with respect to the matrix i.e. electric transport is preferentially channeled along extension defects<sup>38</sup>. It is worth mentioning that the insulator-metal transition occurs in many materials, e.g. it has been reported that the resistivity of  $\text{Bi}_2(\text{AE})_2\text{Co}_2\text{O}_y$  (AE = Ca, Sr, Ba) decreases when AE changes from Ca to Ba, the metal-insulator transition in this material system is observed<sup>39</sup>.

At least two factors indicate the possibility of resistive-switching occurring in NBT single crystals when performing current-voltage characteristics: (1) the occurrence of current oscillations, which can be classified as a kind of unipolar self-switching (Fig. 5i), and (2) the presence of a network of dark stripes on the sample, which can be related to the carriers (oxygen) transport and current paths evolving throughout the sample<sup>38</sup> (Fig. 5j).

### Direct current conductivity results

Figure 6 shows direct current conductivity  $\sigma_{dc}$  vs.  $1000/T$  of NBT single crystals. As marked in this Figure, the  $\sigma_{dc}(1000/T)$  curve consists of five linear sections (ranges). The characteristic temperatures of NBT have been indicated by arrows. The activation energy  $E_a$  in these ranges was determined based on the Arrhenius equation:

$$\sigma_{dc} = \sigma_0 \exp\left(\frac{-E_a}{k \cdot T}\right) \quad (6)$$

where:  $\sigma_0$  – pre-exponential factor,  $k$  – Boltzmann constant,  $T$  – temperature. The obtained activation energies are presented in Table 2.

The determined  $E_a$  values (Table 2) show that the electrical conductivity in NBT is complex and depends on the temperature range. At low temperatures, two competing conduction mechanisms coexist: the band model and the hopping model. The first one describes the phenomenon of conduction of quasi-free electrons and holes



in the appropriate bands. The lowest  $E_a$  values recorded in the ferroelectric phase (up to about 200 °C) result from the dominant mechanism of the conduction phenomenon of quasi-free electrons and holes, which is confirmed by studies of the thermoelectric properties of the Seebeck effect (see below). The change in the activation energy value around the depolarization temperature ( $T_d \approx 190$  °C) indicates a change in the conduction mechanism<sup>21</sup>. The activation energy values ( $\sim 0.4$  eV) occurring in the region of coexistence of the rhombohedral and tetragonal phases (200–350 °C) can be associated with the increasing contribution to the conductivity of small polarons, as a result of their interaction with phonons, and eventually with a gradual change of oxygen vacancies from a neutral to a singly ionized state. Above  $T_m$ , the  $E_a$  value increases several times, which suggests that conduction at higher temperatures may occur through oxygen vacancies. In the highest range of temperatures tested, we observe a decrease in the  $E_a$  value, which suggests an increase of the electron conductivity contribution to total conductivity. To summarize, the NBT activation energy values in the presented temperature ranges are the result of various mechanisms of transport of electric charge carriers.

### Depolarization current results

Depolarization currents for samples polarized at different temperatures, times and electric fields are shown in Fig. 7. In general, three components with different angles of inclination and one nonlinear component can be distinguished, except Fig. 7d, where four components are visible for temperature 170 °C. The first nonlinear component which appears is directly related to the domain reorientation process, and the others are related to various types of polarization, including ionic, dipole and electronic<sup>40</sup>. Localized states (potential centers), e.g. ferroelectric/ferroelastic domain walls, point defects and inhomogeneity of the distribution of ions, which causes some occurrence of disorder in NBT. The latter is usual in perovskites with complex compositions such as NBT. Free charges as well as charges injected from electrodes at high electric field may be trapped on these centers. For example, an oxygen deficiency occurs in NBT (see XPS data), which leads to the appearance of long-range potential centers. After switching-off the applied electric field, charges which were trapped on localized states are released. This means that the sample is subjected to depolarization current flows through the sample<sup>32</sup>. Due to technical limitations, it was not possible to measure currents in the temperature range 200–300 °C, where rhombohedral and tetragonal phases coexist. At higher temperatures, charge transport between potential centers will play a significant role in both polarization and depolarization processes, as well as electrical conduction<sup>41</sup>.

The changes in discharge currents were described by the equation:

$$I_d \sim t^{-s} \quad (7)$$

where  $I_d$  - depolarization (discharge) current intensity,  $t$  - time,  $s$  - exponent (dependent on polarization time and temperature)<sup>42</sup>. At the beginning of the depolarization process, the parameter  $s$  is approximately equal to zero, and then takes on larger values over time, eventually reaching or exceeding the value of one. The slope of the graph increases as the value of the polarization field increases, so the parameter  $s$  takes on larger and larger values. Similar results were obtained for NBT ceramics<sup>42</sup>.

The course of changes in the value of the total depolarization charge  $Q_d$  depending on the discharge time at selected temperatures is shown in Fig. 8. The highest increase in the  $Q_d$  value is recorded in the first seconds of the depolarization process. As the temperature increases, the charge  $Q_d$  takes on higher values, which results mainly from the increased mobility of the charge.

### Alternating current conductivity results

The alternating current conductivity  $\sigma_{ac}$  is related to the total conductivity  $\sigma_t$  and the direct current conductivity  $\sigma_{dc}$  by the relationship<sup>18</sup>:

$$\sigma_t(\omega) = \sigma_{ac}(\omega) + \sigma_{dc} \quad (8)$$

where  $\omega = 2\pi f$  is the angular frequency.

Figure 9a shows changes of the  $\sigma_{ac}$  and  $\sigma_t$  for selected frequencies (0.1, 1 kHz and 2 MHz) vs.  $1000/T$  during heating. The values of  $\sigma_{ac}$  are significantly greater than  $\sigma_{dc}$  (Fig. 6), indicating that the total conductivity is predominantly influenced by  $\sigma_{ac}$ . With increasing frequency, the contribution of the alternating current decreases. So,  $\sigma_{dc}$  contributes to the overall conduction only in measurements conducted at low frequencies. The ac conduction depends on the temperature and frequency of the electric field and is related to the movement of charge carriers at short-range scales. At low frequencies, the action of the electric field on charge carriers lasts for a long period of time. This favors the formation of localized states of these carriers and their elimination from the transport process, which results in lower conductivity in this frequency range. Anomalies of  $\sigma_{ac}$  ( $1000/T$ ) plot are visible around  $T_d$  and  $T_m$ . The increase in the ac conductivity value may be caused by an increase in the concentration of electric charge carriers and/or an increase in their mobility. This indicates a thermally activated conduction process typical of the hopping mechanism of small polarons which proves the semiconductor features of NBT. Note that for frequencies  $f < 2$  kHz and for  $T > 200$  °C conductivity grows rapidly (exponentially) on heating (a nearly linear interval appears in the Arrhenius plot), which reflects a growing contribution of thermally activated charges. The obtained conductivity values are consistent with literature data<sup>21</sup>.

To better illustrate the temperature changes of ac conductivity, a graph of  $\sigma_{ac}$  as a function of temperature for selected frequencies is presented in Fig. 9b. In the low temperature range up to approximately 140 °C, a thermally activated increase in conductivity is observed, the rate of this increase depends on the frequency. The local increase in conductivity in the temperature range 170–190 °C is related to the process of sample depolarization. Above a temperature of 190 °C, there is a significant reduction in the conductivity value due to the coexistence of phases. Subsequently, an associated increase in  $\sigma_{ac}$  is observed with the dominant thermally activated mechanism

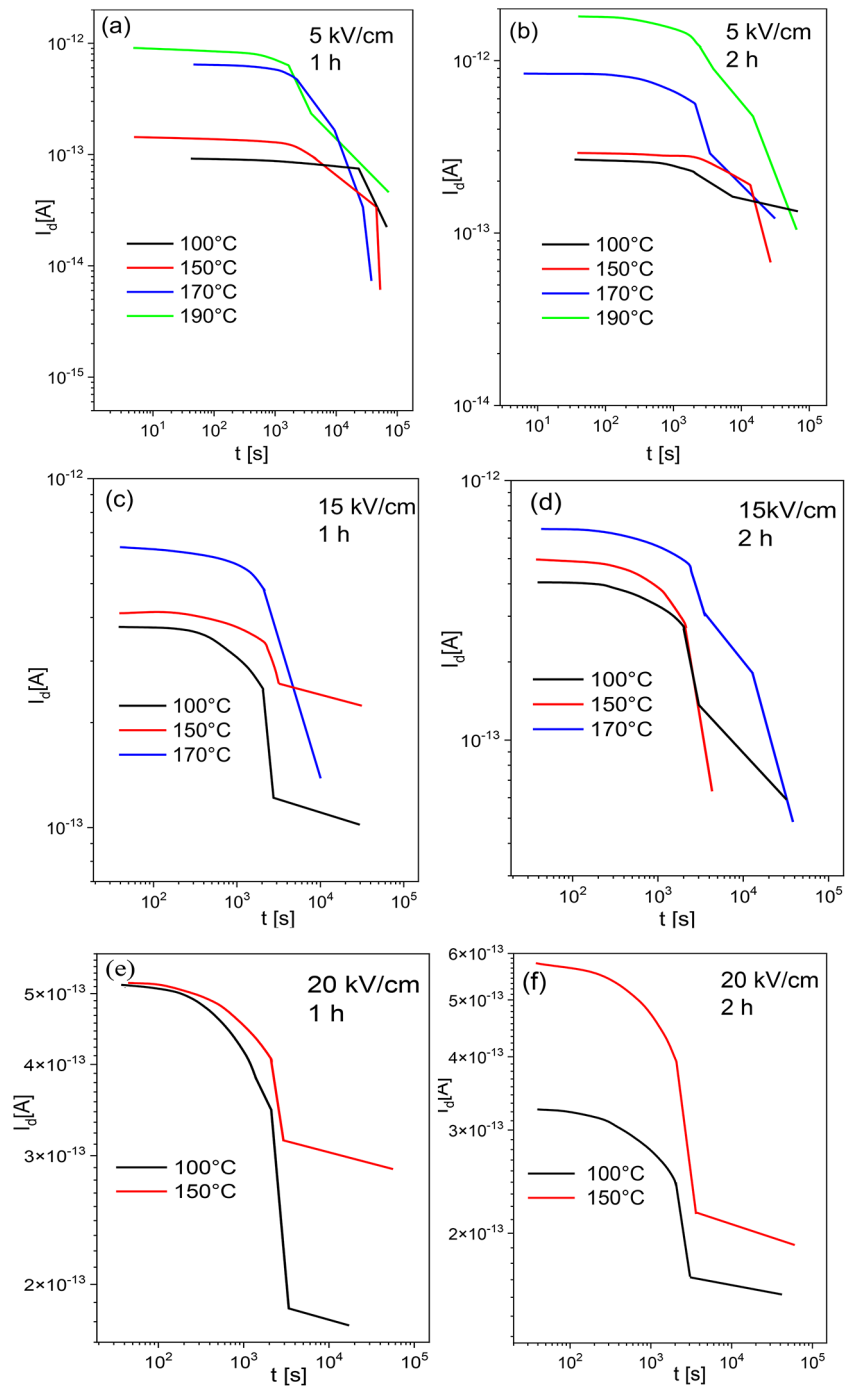


**Fig. 7.** Depolarization currents of NBT single crystals at several temperatures and for polarization time 1 and 2 h.

and the formation of a tetragonal phase. It should be mentioned that the local increase in the  $\sigma_{ac}$  value observed in the temperature range of 320–330 °C is correlated with the disappearance of the domain structure and the existence of the maximum of electric permittivity. The anomaly around the temperature of 400 °C is related to the contribution of hopping conductivity and possibly an increase in the contribution of ionic conductivity. A  $\sigma_{ac}(T)$  anomaly is also present around the temperature of 540 °C, correlating with the T-C phase transition. In the above analysis, the following temperatures were once again distinguished:  $T_d$ ,  $T_m$  and  $T_{T-C}$ . It should also be mentioned, that comparison of both  $\sigma_{ac}(T)$  and  $\sigma_{dc}(T)$  dependencies points to the contribution of dielectric losses to  $\sigma_{ac}$  conductivity.

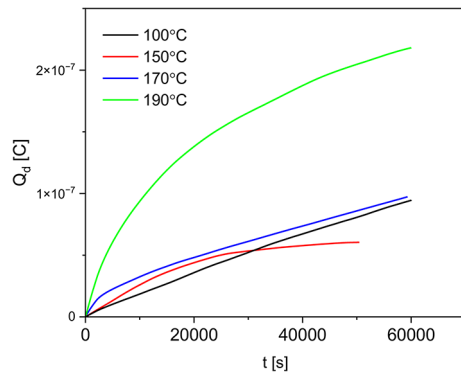


**Fig. 8.** The total depolarization charge  $Q_d$  of NBT single crystals at different temperatures.

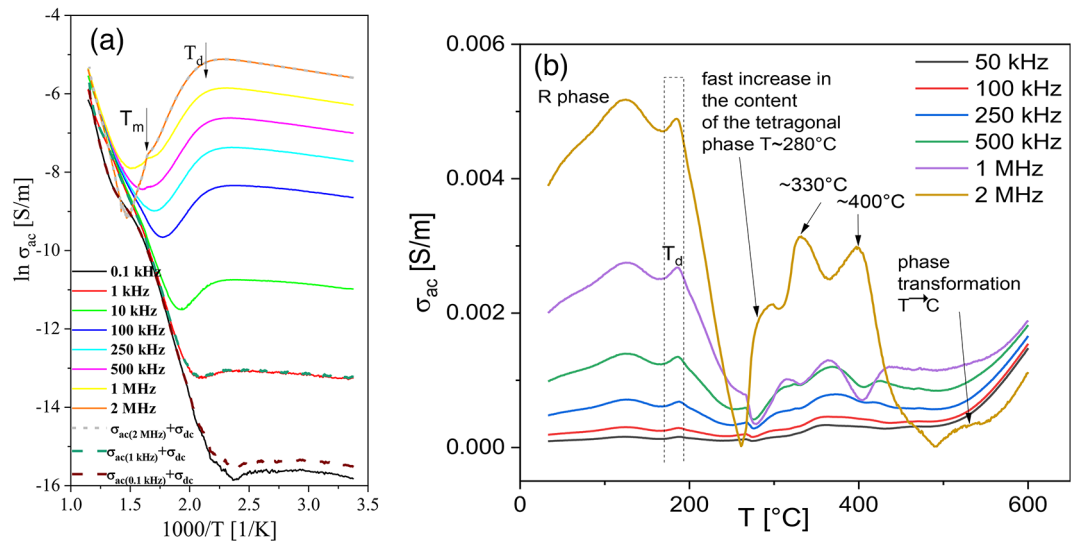


**Fig. 9.** ac conductivity  $\sigma_{ac}$  vs.  $1000/T$  (a) and ac conductivity  $\sigma_{ac}$  vs.  $T$  (b) of NBT single crystals. Two vertical dotted lines in (b) indicated the depolarization phenomenon (i.e. disappearance of polar (ferroelectric) properties). The dash lines show total conductivity calculated according Eq. (8).

### Complex impedance spectroscopy analysis

Figure 10 shows Nyquist plots  $Z''(Z')$ , in which the  $-Z''$  and  $Z'$  axes refer to the imaginary and real parts of the impedance, respectively. The obtained spectra have an overall shape resembling two semicircles whose maximum radius decreases with increasing temperature. The specificity of changes in the  $Z'$  value as a function of temperature is characteristic of semiconductor materials. Seen in detail, the EIS spectra have the form of two partially separated semicircles. The first semicircle present in the high-frequency region (0.1–10 MHz) could come from the sample (Fig. 10a) and the second one from double-layer capacitance occurring at the electrode-single crystal interface (Fig. 10b)<sup>43</sup>. The second semicircle shows the highest impedance contribution and is located at medium and low frequencies between 10 kHz and 10 Hz. The analysis uses an electric equivalent circuit (EEC) composed of a parallel connection of a resistor  $R$  and a capacitor  $C$  or a constant model element (CPE) based on simple RC-RC model (EEC). Nevertheless, several different EEC models were taken into consideration to fit the EIS spectra obtained. The  $R_1$  value is responsible for the resistance of the single crystal, and  $C_1$  for its capacity, and  $R_2$  value is related to the resistance of the interface phenomena, and  $C_2$  for its capacitance at a given temperature<sup>44</sup>. The values of the total electric resistance  $R_1$  of sample were estimated based on EEC model. The EEC fitting lines are shown in the Fig. 10b. The evolution of  $R_1$  values in function of inverse temperature is presented in Fig. 10c. The  $R_1$  parameters obtained from the EIS fitting procedure showed the thermal activation process.

The activation energy  $E_a$  was determined (based on  $R_1$  data) as 1.19 eV using the Arrhenius formula in the temperature range from 475 to 600 °C by fitting a straight line to the collected experimental data (Fig. 10c). The value of this activation energy and values of dc conductivity activation energies (1.18 and 1.14 eV) indicate that oxygen vacancies should be the most probable electric charge carriers in high-temperature range. On the other hand, the relationship between the width of the optical bandgap and the activation energy  $E_g \sim 2E_a$ , suggests that the conduction mechanism is consistent with intrinsic electronic conduction (i.e. the Fermi level is close to the

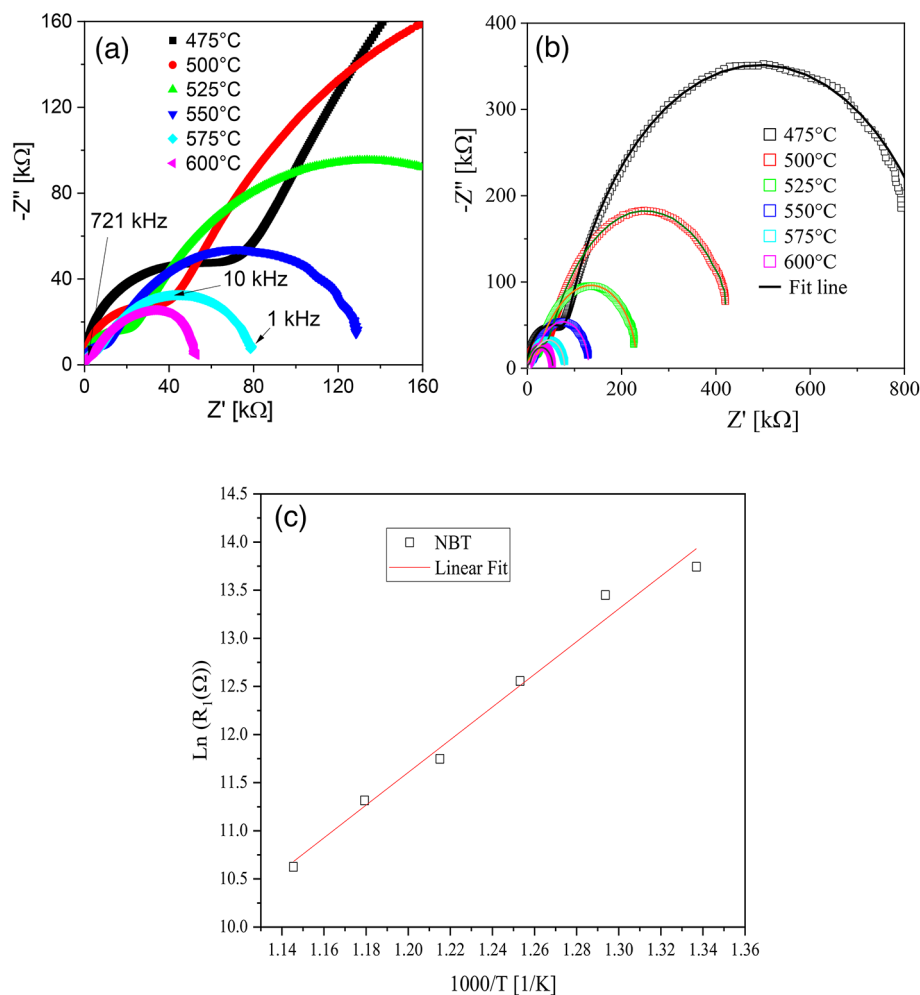


**Fig. 10.** Nyquist plot of NBT single crystals at selected temperatures, for small  $Z'$ ,  $Z'$  ranges (a) and for full  $Z'$ ,  $Z'$  ranges (b). The solid line represents the data fitted using the equivalent circuit model. The evolution of values  $R_1$  in function of inverse temperature (Arrhenius plot) (c).

midgap energy) in the analyzed temperature range. These results indicate two types of charge carriers, i.e. oxygen vacancies and electrons, in the electric conductivity process. In turn, research conducted in papers<sup>42,45</sup> showed that an activation energy above 2 eV is required for ion migration in NBT. However, this value of the activation energy is only valid for a stoichiometric material, because any non-stoichiometry, particularly in the oxygen sublattice (e.g. oxygen loss), will lower this energy<sup>46</sup>.

Further analysis of the conduction mechanism includes tracking changes in the real  $Z'$  and imaginary component  $-Z''$  as a function of frequency at selected temperatures (Fig. 11). The real component  $Z'$  (Fig. 11a) shows a sigmoidal evolution vs. frequency in the low-frequency region followed by a saturation region in the high-frequency region. In the examined temperature region of 100–600 °C, the  $Z'$  values were observed to be greater at lower frequencies. In the low-frequency region (under 10 kHz), it was observed that  $Z'$  values diminished as the temperature rises from 400 °C to 600 °C. It can be also observed that over 400 °C, peak positions shift to higher frequencies with increasing temperature. This suggests a decrease in the resistance of the bulk and electrode interface, which in turn implies an enhancement in the sample conductivity. However, the curves from various temperatures converged to a nearly plateau region at higher frequencies (above 100 kHz) (the arch-like region progressively shrinks with increasing temperature for the temperature interval above 300 °C and for high frequencies the creep-like region becomes predominant, insert in Fig. 11a). This phenomenon can be attributed to release of point defects (space charge)<sup>47</sup>. The distinguishing features are the emerging modes (maxima) in the region of intermediate frequencies related to by the electrode-sample interface.

The imaginary part  $Z''$  of impedance as a function of frequency at different temperatures is shown in Fig. 11b. The plots exhibit two peaks: one at lower frequencies and a second one at higher frequencies. The major one is related to the electrode-surface phenomena, and the second peak originates from the sample bulk. The minor peak related to the crystal shifts towards high frequencies with increasing temperature, while its amplitude gradually diminishes. The peak indicates the maximum dielectric loss at the given frequency and attains a constant value in the high-frequency region. For frequencies below this peak, dipoles are completely polarized or aligned along the applied ac electric field and are in a stretched state. These observations show that the sample's

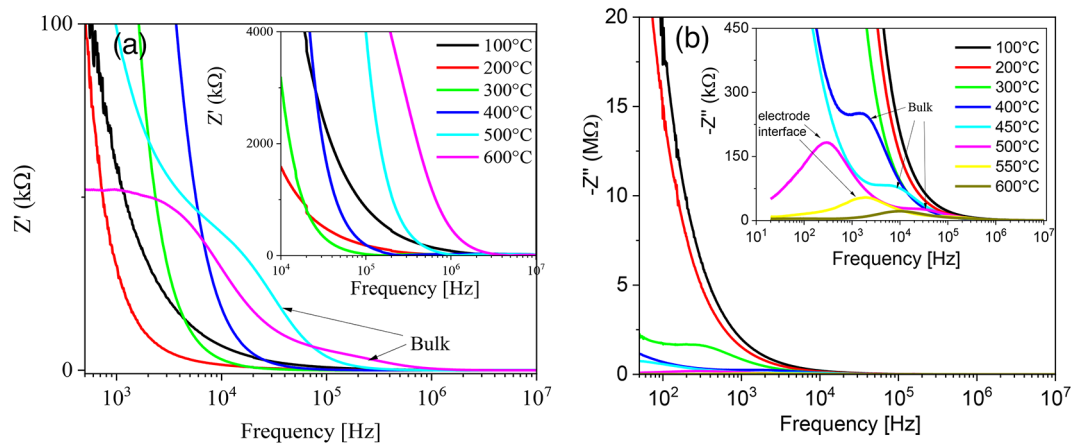


**Fig. 11.** Changes of  $Z'$  and  $Z''$  as a function of frequency at selected temperatures.

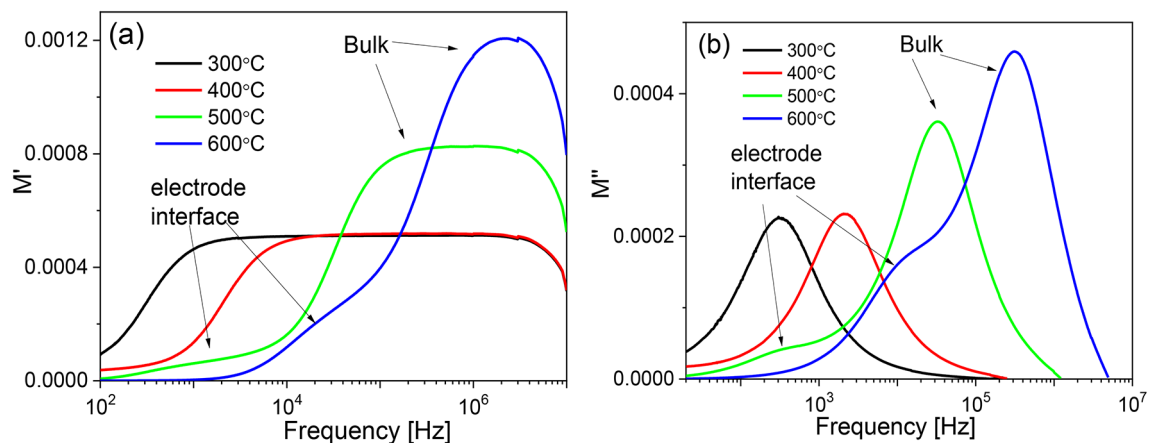


**Fig. 12.** The frequency dependence of the  $M'$  and  $M''$  modules of NBT single crystals for selected temperatures.

resistive properties were reduced and indicate the occurrence of relaxation processes in this temperature range. As temperature increased, thermal energy  $k_B T$  provides driving force to the movement of charges. A detailed shape analysis suggests that we are dealing with only one relaxation process from the sample.

The complex electric modulus  $M$  (real component  $M'$  and imaginary  $M''$ ) is the inverse of the complex permittivity, which is used to study dielectric relaxation processes in materials. The frequency dependences of  $M'$  process is shown in Fig. 12a.  $M'$  has very low values at lower frequencies and exhibits an increasing trend with the rise in frequency. When  $M'$  approaches zero this behavior confirms the presence of an appreciable electrode and/or ionic polarization and represents an absence of the restoring energy for the mobile charge carriers in the studied temperature ranges. Generally, in the entire frequency range, the  $M'$  values decrease with increasing temperature up to  $\sim 400^\circ\text{C}$ . Above this temperature, the  $M'$  values increase significantly with further temperature increase, especially in the high frequency range, resulting in a change in the dispersion image. This effect can be related to the increasing importance of ionic conductivity at high temperatures.

For high temperatures, a significant increase in  $M'$  is observed with increasing frequency. Next, there is a “plateau” area where electrical processes are frequency independent. This area narrows as the samples are heated further. As the temperature increases, the slope of the  $M'(f)$  curves shifts towards higher frequencies, which is reflected in decreasing relaxation times. This phenomenon results from the increased activation of the short-range mobility of charge carriers or a gradual decrease in electron-lattice coupling<sup>28,30</sup>.

$M'$  almost reaches zero at low frequencies due to the lack of electrical polarization and high dielectric losses and represents an absence of the restoring energy for the mobile charge carriers.  $M'$  tends to reach a maximum (saturation) at high frequencies. This saturation can be connected to the fact that charge carriers move within a reducible range until the electric field changes become too rapid to induce the oscillation of charge carriers (vacancies).

Figure 12b shows the changes in the imaginary part of the electrical modulus  $M''$  as a function of frequency, which denotes energy loss in the presence of an electric field. The evolution of  $M''$  shows that with increasing temperature the maxima (peaks) shift to higher frequencies, which indicates that charge carriers become

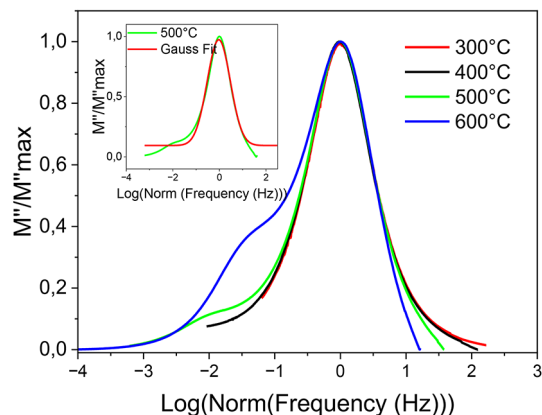


**Fig. 13.** The normalized imaginary part of the  $M''/M''_{\max}$  module for NBT single crystals.

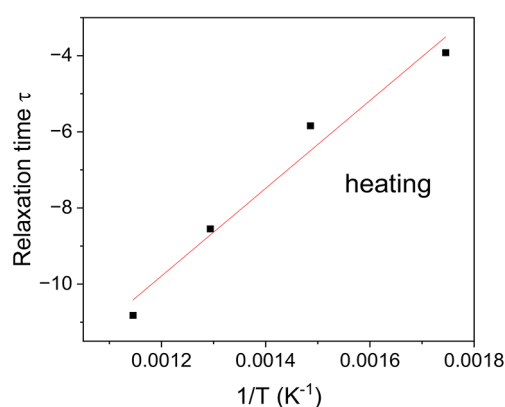


**Fig. 14.** Evolution of the conduction relaxation time as an inverse function of the temperature for NBT single crystals.

thermally stimulated with increasing temperature, resulting in a gradual movement (in other words: increasing temperature trigger faster ionic activity, which results in the peak shifting towards higher frequencies). The shorter period and increase of the relaxation frequency, suggests the presence of a temperature-dependent thermally activated relaxation process, dominated by the charge carrier hopping mechanism<sup>48</sup>. In the low-frequency interval below the maximum of  $M''(f)$ , carriers can hop from one site to another site (i.e. long-distance hopping exists). In the high-frequency interval above the maximum of  $M''(f)$ , charge carriers move over a short distance (i.e. localized movement inside potential wells). At the same time, the broadening of the asymmetric peak of  $M''(f)$ , particularly at higher temperatures can be ascribed to non-Debye type relaxation (a stretched exponential character of the relaxation time exists) and is typical of hopping ion conductivity<sup>49–51</sup>.

Figure 13 shows the normalized imaginary part of the  $M''/M''_{\max}$  modulus as a function of frequency ( $\log \text{norm}(f/f_{\max})$ ) in a wide temperature range. The frequency was normalized to the point where  $M''(f)$  reaches the maximum value  $M''_{\max}$ . There is one overlapping relaxation curve with perturbations in the low-frequency region (left side) originating from the electrode-sample interface. This clearly suggests the same activation energy of oxygen vacancies occurring on different time scales and that the distribution of the relaxation times is temperature independent. A good fit of the experimental curves with a Gaussian function is also shown (insert in Fig. 13). The value of FWHM evaluated from the normalized spectrum is greater than  $\log[(2 + \sqrt{3})/(2 - \sqrt{3})]$ , and this indicates non-Debye-type behavior, which is supported by the complex impedance and modulus plots.

The evolution of the conduction relaxation time as an inverse function of the temperature is shown in Fig. 14. The most probably relaxation time  $\tau$  is estimated from the position of  $M''_{\max}$  as a function of frequency, according to the relationship<sup>47</sup>:

$$t = 1/2\pi f \quad (9)$$

where  $f$  is the relaxation frequency at the point  $M''_{\max}$ .

The activation energy ( $E_{a-rel}$ ) in the conductivity relaxation was calculated from the modified Arrhenius equation:

$$\tau = \tau_0 \exp(E_{a-rel}/kT) \quad (10)$$

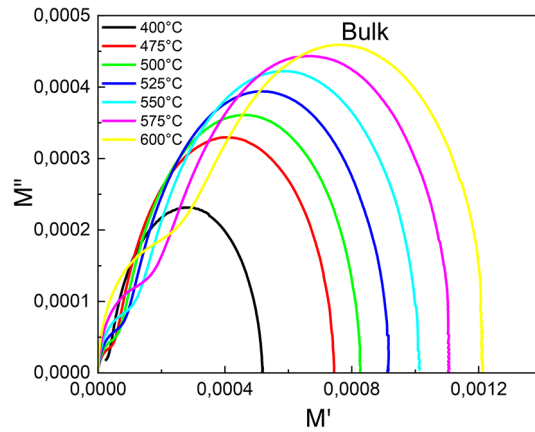


**Fig. 15.**  $M'$  vs.  $M''$  of NBT single crystals.

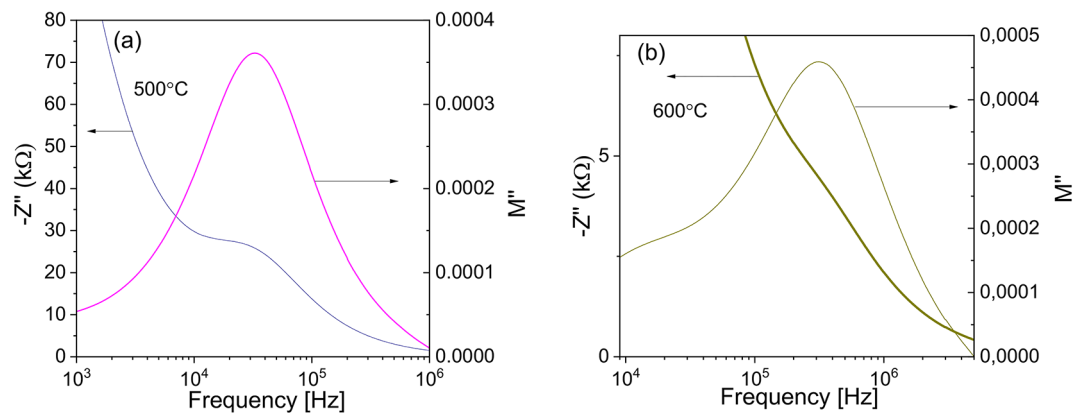


**Fig. 16.** Variation of  $Z''$  and  $M''$  with frequency of NBT single crystals (as a examples).

$$\tau = \tau_0 \exp(E_{a-rel}/kT) \quad (10)$$

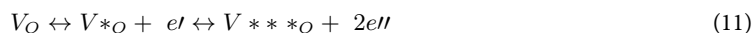
where:  $\tau_0$  is the pre-exponential factor and is equal  $5.6 \times 10^{-11}$  s for NBT single crystals.

The activation energy for conductivity relaxation ( $E_{a-rel}$ ) is equal to the free energy of charge carrier migration (hopping) between adjacent positions in the lattice<sup>52,52</sup>. However, the activation energy obtained from dc conductivity is the sum of both the creation and migration free energy of charge carriers. It was found from Eq. (10) that  $E_{a-rel}$  is equal 0.99 eV. The closeness of this activation energy to those obtained from dc conductivity (1.18 and 1.14 eV) indicates that dispersion of the conductivity is attributable to the hopping of charge carriers. Based on these results, we can conclude that the creation free energy should be close to zero, which suggests that the carrier concentration is temperature independent, i.e. the carriers are almost dissociated from traps. These activation energies are comparable to the activation energy of 0.8–1.1 eV obtained for diffusion of oxygen vacancies in perovskite oxides<sup>53,54</sup>. Such values of the activation energy for NBT single crystals are indicative of the ionic nature of the electric relaxation involved in the process.

The next stage of the research was the analysis of the Argand chart ( $M'$  vs.  $M''$ ) and the results are shown in Fig. 15. It is observed that the average radius of the arcs increases with increasing temperature, and the maximum values of  $M''_{max}$  shift to the higher frequency area. This confirms that relaxation is a thermally activated process dominated by the charge carrier hopping mechanism. As expected, only one semicircle dominates in the tested material, and the presence of small additional ones probably results from processes occurring at the crystal-electrode interface.

Figure 16 shows the combined diagram of  $Z''$  and  $M''$  versus frequency. The peak  $Z''(f)$  and  $M''(f)$  do not overlap, which indicates that the relaxation process is dominated by the short-range movement of charge carriers (relaxation time is temperature independent) and departs from the Debye type conduction mechanism found from Fig. 14<sup>55–57</sup>. This also suggests that the conduction process may be localized<sup>58</sup> in accordance with the above-mentioned prediction.

In oxide perovskites, oxygen vacancies ( $V_O$ ) are thought to be one of the mobile charge carriers. In the NBT crystal, oxygen vacancies are generated by trace impurities of the reagents as well as the evaporation of Bi ions during processing of the material. In general, they can occur in three states: the neutral state  $V_O$  ( $V_O^0$ ), the singly ionized  $V^* O$  ( $V_O^{2+}$ ) state, and the doubly ionized  $V^{**} O$  ( $V_O^{2+}$ ) states. The neutral-state vacancies may be thermally ionized to singly ( $V^* O$ ) and doubly ( $V^{**} O$ ) ionized states according to:



Conduction electrons released from neutral oxygen vacancies may be trapped (localized) by  $Ti^{4+}$  ( $Ti'_{Ti}$  centers) and this generates a reduction of the valence following the relation:



Besides their association with Ti, these electrons can be weakly bonded (trapped) to oxygen vacancies, which can form a shallow level to trap electrons. However, it is difficult to detect the precise location of the electrons, because this process can depend on the local structure and temperature. Deficiency of electrons in p-type NBT (see below) favors the ionization of oxygen vacancies. The energy levels of  $Ti'_{Ti}$  centers are also shallow, and the electrons can easily hop via titanium ions contributing to charge transport. The thermal activation of the electrons trapped by this Ti or by oxygen vacancies can increase conduction. The electron hopping may take two pathways (i) direct hopping in an oxidation-reduction process between Ti ions according to relation (12), and (ii) jumping through the bridging oxygen vacancies between Ti ions according to relation (11). Activation energies for singly and doubly ionized oxygen vacancies are in the ranges 0.3–0.5 and 0.6–1.2 eV, respectively<sup>59–61</sup>, which suggested that, in our studies, double-ionized oxygen vacancies will be the dominant way of generating conductivity in the higher temperature range than single ionized ones. The oxygen vacancies, electrons localized on titanium ions<sup>62,63</sup> and probably associated complexes based on them ( $Ti'_{Ti}-V^{**}O$ )<sup>\*</sup> could be the more likely charge carriers involved in the conduction process in the high-temperature range conductivity of NBT single crystals. The associated complexes are rather unstable and gradually decompose during heating, releasing their more mobile components, which participate in the charge transfer. We should also remember the possibility of the recapture of the previously emitted electrons by oxygen vacancies. This can be due to oxygen vacancies becoming metastable at high temperatures. Thus, the conduction process can occur due to the hopping of electrons between  $Ti^{4+}$  and  $Ti^{3+}$ , leading to the contribution of both single and doubly ionized oxygen vacancies and to the contribution of the hopping energy between these localized centers to the activation energy in the high-temperature range. The decrease of the dc conductivity activation energy from 1.26 eV to 1.18 eV at 450 °C and from 1.18 eV to 1.14 eV at 553 °C can be related to an increased concentration of doubly ionized vacancies and/or to increased electron content. In summary, these results show that oxygen vacancies and hopping electron mechanism coexist in NBT single crystals and make an important contribution to the electric conductivity and determine the conduction relaxation process in the high-temperature range.

The oxide-ion conduction in NBT may originate from (i) Bi deficiency and oxygen vacancies created during the material processing<sup>21</sup>, and (ii) the highly polarizable  $Bi^{3+}$  ion, which provide pathways with low diffusion barriers, favoring the migration of oxygen ions<sup>42,43,64</sup>. Ion migration can result in, among other things large leakage currents<sup>65</sup>, which is observed in NBT. In the low-temperature range, trapping of oxygen vacancies and their association with Bi vacancies makes their migration difficult or impossible and they do not contribute markedly to the long-range conduction process. In addition, most of the oxygen vacancies should be neutral in thermal equilibrium in this temperature interval due to the deep defect level, i.e. the Fermi level can be located above the defect level of the oxygen vacancy. However, as the temperature increases, due to the supplied thermal energy, the trapping energy gradually decreases and oxygen vacancies are released from the traps, gradually becoming ionized and releasing electrons. These vacancies and electrons contribute increasingly to electrical conductivity.

Complex impedance spectroscopy measured at high-temperatures captures the superposition of the electronic and ionic conductivity contributions. The contribution of electrons to charge carrier transfer, particularly in the high-temperature range can be related to the nonstoichiometry of NBT. As mentioned above, bismuth deficiency is one of the reasons for formation of oxygen vacancies in NBT. However, in our samples an excess of bismuth occurs. In this situation, a smaller number of oxygen vacancies and, consequently the emergence of electronic conductivity, should be expected. On the other hand, deficiency in sublattice O also occurs (see XPS results). The competitive influence of these non-stoichiometries may lead to an imbalance in the proportions between ionic and electronic conductivities. These results show that the possibility exists of modeling NBT single crystals with desired properties (particularly the expected electric conductivity) through careful control of stoichiometry, which can be achieved by minute selection and examination of the precursors and detailed control/steering of crystal growth conditions.

### Thermoelectric results

Figure 17a shows the temperature dependence of the Seebeck coefficient  $\alpha$ . The  $\alpha$  value generally increases with increasing temperature over the entire temperature range. The nearly temperature-independent Seebeck coefficient up to about 200 °C suggests that the carrier mobility is thermally activated in this temperature range, which indicates the hopping process as discussed above. At higher temperatures, two distinct local maxima of  $\alpha(T)$  are visible around the temperatures characteristic for NBT. The first anomaly visible around 190–220 °C is related to the disappearance of the long-range ferroelectric properties (depolarization process). The second maximum is visible in the temperature range of 220–350 °C, in which rhombohedral and tetragonal phases coexist. At the same time, in this temperature range there is a gradual process of changing symmetry from rhombohedral to tetragonal. The positive sign of the Seebeck coefficient indicates the dominance of p-type conductivity. This can be due to creating of holes  $h^+$  during cooling after growing or during the annealing step according to reaction:





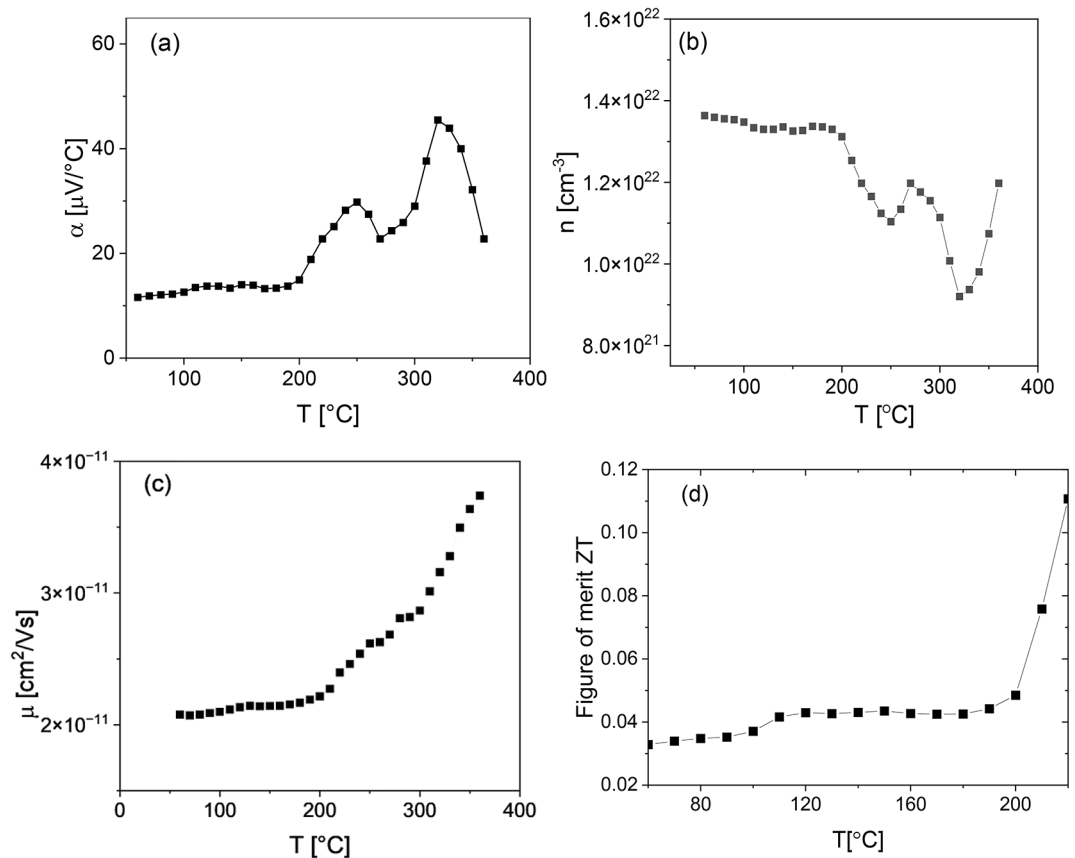


**Fig. 17.** The temperature dependence of (a) the Seebeck coefficient  $\alpha$ , (b) carrier concentration  $n$ , (c) carrier mobility  $\mu$ , and (d) figure of merit  $ZT$  of NBT single crystals.

The holes have higher mobility than oxygen vacancies.

Based on experimental data and on Eqs. (14) and (15), the carrier concentration  $n$  and carrier mobility  $\mu$  were calculated<sup>66,67</sup> as:

$$\alpha = k_B/e \ln(N_c/n) \quad (14)$$

where  $k_B$  – Boltzmann constant,  $e$  – electric charge of the carrier,  $N_c$  – effective density of states in the conduction band (for NBT  $N_c = 1.56 \times 10^{28} \text{ m}^{-3}$ ),  $n$  – carrier concentration.

$$\sigma = en\mu \quad (15)$$

where:  $e$  – electric charge of the carrier, and  $\mu$  – mobility of the carrier. The results obtained are presented in Fig. 17b, c.

The temperature dependence of thermoelectric power factor was determined in terms  $(\alpha^2\sigma)/\kappa$  and shown in Fig. 17d. As can be seen, the value of the power factor increases with increasing temperature. However, its values are too low (particularly in the low-temperature range) for actual use as a thermoelectric module. This may be due to the high resistivity (low electric conductivity) and high thermal conductivity. Although it is simple to increase the electric conductivity of NBT through introduction of non-stoichiometry (increased concentration of defects)<sup>42,68</sup>, such a strategy usually also results in an undesirable increase of thermal conductivity. Thus, achieving a reasonable compromise between the value of both parameters in a simple way is difficult in pure NBT.

### Thermal conductivity results

Temperature variation (RT–220 °C) of thermal conductivity ( $\kappa$ ) is shown in Fig. 18a. The small anomaly of  $\kappa(T)$  at about 140 °C is visible (indicated by an arrow). Note that an anomaly in the DSC(T) plot was detected at similar temperature<sup>67</sup>. The thermal conductivity can be described as a sum of the lattice  $\kappa_l$  and electronic  $\kappa_e$  contributions<sup>69</sup>:

$$\kappa = \kappa_l + \kappa_e \quad (16)$$

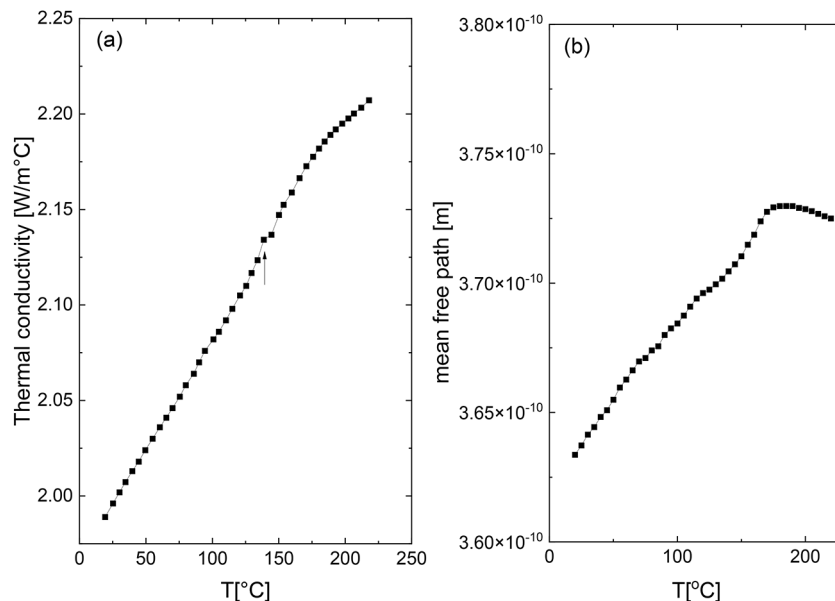


**Fig. 18.** Temperature evolution of (a) thermal conductivity and (b) average mean free path of NBT single crystals.

To separate  $\kappa_l$  from  $\kappa_e$ , the electronic thermal conductivity was calculated using Wiedemann-Franz law  $\kappa_e = L\sigma T$ , where a Lorentz number of  $L = 2.44 \times 10^{-8} \text{W}\Omega\text{K}^{-2}$  was taken, and  $\sigma$  is the electrical conductivity. The lattice thermal conductivity  $\kappa_l$  can then be derived by subtracting  $\kappa_e$  from  $\kappa$ . This estimation shows that the phonon thermal conductivity of NBT single crystals is predominant in the total thermal conductivity. Note that dc electric conductivity is in the range of  $10^{-11}$ - $10^{-12} \text{S}\text{m}^{-1}$  in the investigated temperature interval. This indicates that the contribution of free electrons to the thermal conductivity is small, which confirms the predominantly phonon nature of the thermal conductivity of the investigated material. In general, thermal conductivity increases up to about 190 °C (depolarization temperature) and then tends to stabilise with further temperature increase (Fig. 18a). Assuming that the dominant contribution to thermal conductivity originates from phonons, their dispersion on domain walls (in the range in which the ferroelectric phase exists) and, interphase boundaries (in the range of coexistence of rhombohedral and tetragonal phases) may determine the total thermal conductivity. These perturbations of crystal structure lead to an increase of collisions of phonons travelling through the lattice (i.e. the thermal phonon scattering increases) which can reduce the lattice thermal conductivity. Thermal conductivity ( $\kappa$ ) directly depends on the concentration of carriers, i.e. when the carrier concentration increases,  $\kappa$  also increases. However, it is difficult to independently consider all factors, which influence the thermal conductivity, because they are interrelated<sup>70</sup>.

It is expected that the perturbations of crystal structure can lead to a shortening of the phonon mean free path. The phonon mean free path was calculated using the relation:

$$\kappa = 1/3 C_v \vartheta l \quad (17)$$

where  $C_v$  is the heat capacity per unit volume<sup>71</sup>,  $\vartheta$  is the average sound velocity and  $l$  is the average phonon mean free path. Average sound velocity was measured using the usual pulse echo technique<sup>14</sup>. Temperature evolution of the calculated average mean free path is shown in Fig. 18b. In general, the average phonon mean free path increases up to about 190 °C (depolarization temperature) and then tends to stabilise with further temperature increase. The average phonon mean free path is comparable to the lattice parameters of NBT presented in papers<sup>72,73</sup>.

## Conclusions

Lead-free  $\text{Na}_{0.5}\text{Bi}_{0.5}\text{TiO}_3$  single crystals were grown by the Czochralski technique. Studies of the thermoelectric effect (Seebeck coefficient), depolarization current, current-voltage characteristics, and direct ( $\sigma_{dc}$ ) and alternating ( $\sigma_{ac}$ ) electrical conductivities for these crystals were performed. Impedance spectroscopy measurements provided a framework for creating an electric conductivity model for NBT. The occurrence of a reversible insulator-metal transition on nanoscales caused by the electric field, was revealed. The following conductivity mechanisms of NBT single crystals were identified: (i) at low temperatures, two competing conduction mechanisms coexist: the band model and the hopping model (with dominance of the first mechanism); (ii) in the middle temperature interval, movement of small polarons; and (iii) in the high temperature interval, hopping of electrons thermally excited from oxygen vacancies. This gives useful pointers to strategies for optimizing the electrical conductivity for specific applications. The decrease of the activation energy in the high temperature range can be explained by an increase of the concentration of doubly ionized vacancies and/or an increased content of electrons. It is



supposed that the relaxation process identified in the high-temperature interval was determined by a space charge polarization mechanism (i.e. oxygen vacancies and electrons localized on titanium ions) rather than by a dipolar one. The Seebeck coefficient measurements show that NBT single crystals have p-type conductivity. The implications of the studies presented in this paper are twofold. First, they given further insight into the mechanisms responsible for electric conductivity of NBT and related perovskite materials. At the same time, they offer a pathway for creating lead-free perovskite materials with expected behaviors and thus enhances their usefulness in the industrial field.

## Data availability

The datasets used and/or analysed during the current study available from the corresponding author on reasonable request.

Received: 4 October 2024; Accepted: 13 January 2025

Published online: 21 January 2025

## References

- Uchino, K. *Ferroelectric Devices* Marcel Dekker. (2000).
- Zachariasz, R. & Bochenek, D. Properties of the PZT type ceramics admixed with barium and niobium. *Arch. Metall. Mater.* **54**, 895–902 (2009).
- Skulski, R., Wawrzala, P., Ćwikiel, K. & Bochenek, D. Dielectric and electromechanical behaviors of PMN-PT ceramic samples. *J. Intell. Mater. Syst. Struct.* **18**, 1049–1056. <https://doi.org/10.1177/1045389X06072356> (2007).
- Bochenek, D. Magnetic and ferroelectric properties of  $\text{PbFe}_{1/2}\text{Nb}_{1/2}\text{O}_3$  synthesized by solution precipitation method. *J. Alloys Comp.* **504**, 508–513. <https://doi.org/10.1016/j.jallcom.2010.05.153> (2010).
- Suchanicz, J. et al. Structural, thermal, dielectric and ferroelectric properties of poled  $\text{Na}_{0.5}\text{Bi}_{0.5}\text{TiO}_3$  ceramics. *Ceram. Int.* **43**, 17194–17201 (2017).
- Aksel, E. et al. Monoclinic crystal structure of polycrystalline  $\text{Na}_{0.5}\text{Bi}_{0.5}\text{TiO}_3$ . *Appl. Phys. Lett.* **98**, 152901 (2011).
- Rao, B. N., Fitch, A. N. & Ranjan, R. Ferroelectric-ferroelectric phase coexistence in  $\text{Na}_{1/2}\text{Bi}_{1/2}\text{TiO}_3$ . *Phys. Rev.* **B87**, 1–8 (2013).
- Dorcet, V., Trolliard, G. & Boullay, P. Reinvestigation of phase transitions in  $\text{Na}_{0.5}\text{Bi}_{0.5}\text{TiO}_3$  by TEM. Part I: first order rhombohedral to orthorhombic phase transition. *Chem. Mater.* **20**, 5061–5073 (2008).
- Trolliard, G. & Dorcet, V. Reinvestigation of phase transitions in  $\text{Na}_{0.5}\text{Bi}_{0.5}\text{TiO}_3$  by TEM. Part II: second order orthorhombic to tetragonal phase transition. *Chem. Mater.* **20**, 5074–5082 (2008).
- Aktas, O., Duclere, J. R., Quignon, S., Trolliard, S. G. & Salje, E. K. H. Polarity of modulated  $\text{Na}_{0.5}\text{Bi}_{0.5}\text{TiO}_3$  and its slow structural relaxation. *Appl. Phys. Lett.* **113**, 0329011–0329014 (2018).
- Suchanicz, J. Behaviour of  $\text{Na}_{0.5}\text{Bi}_{0.5}\text{TiO}_3$  ceramics in the Ac electric field. *Ferroelectrics* **209**, 561–568 (1998).
- VakhrushevSB et al. Phase transitions and soft modes in sodium bismuth titanate. *Ferroelectrics* **63**, 153–160 (1985).
- Suchanicz, A., Roleder, K., Kania, A. & Handerek, J. Electrostrictive strain and pyroeffect in the region of phase coexistence in  $\text{Na}_{0.5}\text{Bi}_{0.5}\text{TiO}_3$ . *Ferroelectrics* **77**, 107–110 (1988).
- Suchanicz, J. Elastic constants of  $\text{Na}_{0.5}\text{Bi}_{0.5}\text{TiO}_3$  single crystal. *J. Mater. Sci.* **37**, 489–491 (2002).
- Sakata, K. & Masuda, Y. Ferroelectric and antiferroelectric properties of  $\text{Na}_{0.5}\text{Bi}_{0.5}\text{TiO}_3$ - $\text{SrTiO}_3$  solid solution ceramics. *Ferroelectrics* **7**, 347–349 (1974).
- Aksel, E. et al. Local atomic structure deviation from average structure of  $\text{Na}_{0.5}\text{Bi}_{0.5}\text{TiO}_3$ : combined x-ray and neutron total scattering study. *Phys. Rev.* **B87**, 1–10 (2013).
- Balagourov, A. M. et al. The rhombohedral phase with incommensurate modulation in  $\text{Na}_{0.5}\text{Bi}_{0.5}\text{TiO}_3$ . *Phase Transit.* **79**, 163–173 (2006).
- Barick, B. K., Mishra, K. K., Arora, A. K., Choudhary, R. N. P. & Pradhan, D. K. Impedance and Raman spectroscopic studies of  $\text{Na}_{0.5}\text{Bi}_{0.5}\text{TiO}_3$ . *J. Phys. D Appl. Phys.* **44**, 355402 (2011).
- East, J. & Sinclair, D. C. Characterization of  $(\text{Bi}_{1/2}\text{Na}_{1/2})\text{TiO}_3$  using electric modulus spectroscopy. *J. Mater. Sci. Lett.* **16**, 422–435 (1997).
- Saradhi, B. V. B., Srinivas, K., Prasad, G., Suryanarayana, S. V. & Bhimasankaram, T. Impedance spectroscopic studies in ferroelectric  $\text{Na}_{0.5}\text{Bi}_{0.5}\text{TiO}_3$ . *Mat. Sci. Eng.* **B98**, 10–16 (2003).
- Suchanicz, J., Kluczevska-Chmielarz, K., Sitko, D. & Jagło, G. Electrical transport in lead-free  $\text{Na}_{0.5}\text{Bi}_{0.5}\text{TiO}_3$  ceramics. *J. Adv. Ceram.* **10**, 152–156 (2021).
- Karpierz, M. et al. Effects of  $\text{PbTiO}_3$  doping on electric properties of  $\text{Na}_{0.5}\text{Bi}_{0.5}\text{TiO}_3$  ceramics. *Phase Transit.* **90**, 65–71 (2016).
- Mandal, B. & Thakur, A. K. Electrode response of  $\text{NaFeTiO}_4$  in aqueous supercapacitor cells. *Ionics* **27**, 1709–1721. <https://doi.org/10.1007/s11581-021-03938-w> (2021).
- Siddiqui, T. A. J. et al. Mesoporous carbon of carbonized human urine waste: a valuable heterogeneous catalyst for chromone and xanthene derivative synthesis. *Catalysts* **10**, 13691–13617. <https://doi.org/10.3390/catal10121369> (2020).
- Cheng, L., Hu, X. & Hao, L. Easily recycled  $\text{Bi}_2\text{O}_3$  photocatalyst coatings prepared via ball milling followed by calcination. *Appl. Phys. A.* **123**, 4431–4437. <https://doi.org/10.1007/s00339-017-1051-x> (2017).
- Zhou, Z., Xiong, P., Liu, H. & Peng, M. Ultraviolet a persistent luminescence of a  $\text{Bi}^{3+}$ -activated  $\text{LiScGeO}_4$  material. *Inorg. Chem.* **59**, 12920–12927. <https://doi.org/10.1021/acs.inorgchem.0c02007> (2020).
- Hou, D. et al. Electrospun sillenite  $\text{Bi}_{12}\text{MO}_{20}$  (M = Ti, Ge, Si) nanofibers: general synthesis, band structure, and photocatalytic activity. *Phys. Chem. Chem. Phys.* **15**, 20698–20705. <https://doi.org/10.1039/C3CP53945H> (2013).
- Łapiński, M. et al. Plasmon-enhanced photoluminescence from  $\text{TiO}_2$  and  $\text{TeO}_2$  thin films doped by  $\text{Eu}_{3+}$  for optoelectronic applications. *Beilstein J. Nanotechnol.* **12**, 1271–1278. <https://doi.org/10.3762/bjnano.12.94> (2021).
- Horvath, H. Gustav Mie and the scattering and absorption of light by particles: historic developments and basics. *J. Quant. Spectrosc. Radiat. Transf.* **110**, 787–799. <https://doi.org/10.1016/j.jqsrt.2009.02.022> (2009).
- Stern, F. Elementary theory of the optical properties of solids. *Solid State Phys.* **15**, 299–408. [https://doi.org/10.1016/S0081-1947\(08\)60594-9](https://doi.org/10.1016/S0081-1947(08)60594-9) (1963).
- Li, L., Li, M., Zhang, H., Reaney, I. M. & Sinclair, D. C. Controlling mixed conductivity in  $\text{Na}_{1/2}\text{Bi}_{1/2}\text{TiO}_3$  using A-site non-stoichiometry and Nb-donor doping. *J. Mater. Chem. C.* **4**, 1–8 (2016).
- Andriyevsky, B. et al. Manifestation of phase transformations in optical spectra of  $\text{Na}_{0.5}\text{Bi}_{0.5}\text{TiO}_3$  crystals between 25°C and 350°C. *Phase Transitions.* **82**:567–575. (2009).
- Zeng, M., Or, S. W. & Chan, H. L. First - principles study on the electronic and optical properties of  $\text{Na}_{0.5}\text{Bi}_{0.5}\text{TiO}_3$  lead free piezoelectrical crystal. *J. Appl. Phys.* **107**, 0435131–0435138 (2010).
- Bousquet, M., Duclère, J.-R., Orhan, E., Boule, A. & Bachelet, C. Optical properties of an epitaxial  $\text{Na}_{0.5}\text{Bi}_{0.5}\text{TiO}_3$  thin film grown by laser ablation: experimental approach and density functional theory calculations. *J. Appl. Phys.* **107**, 104107 (2010).

35. Scott, J. F., Araujo, C. A., Melnick, B. M., McMillan, L. D. & Zuleeg, R. Quantitative measurement of space-charge effects in lead zirconate-titanate memories. *J. Appl. Phys.* **70**, 382–385 (1991).
36. Lampert, M. A. Simplified theory of space-charge-limited currents in an insulator with traps. *Phys. Rev.* **103**, 1648–1656 (1956).
37. Huey, R. M. & Taylor, R. M. K. Anomalous discharges in ferroelectrics. *J. Appl. Phys.* **34**, 1557–1560. <https://doi.org/10.1063/1.1729678> (1963).
38. Sztot, K., Bihlmayer, G. & Speier, W. Nature of the resistive switching phenomena in TiO<sub>2</sub> and SrTiO<sub>3</sub>: origin of the reversible / insulator-metal transition. *Solid State Phys.* **65**, 354–544. <https://doi.org/10.1016/B978-0-12-800175-2.00004-2> (2014).
39. Dong, S. T. et al. Anisotropically electrical property of Anderson insulator state in Bi<sub>2</sub>Ca<sub>2-x</sub>Sr<sub>x</sub>Co<sub>2</sub>O<sub>y</sub> (x = 0.0, 0.5, 1.0, 1.5, 2.0) single crystals. *J. Alloys Comp.* **840**, 15545–15551 (2020).
40. Stanuch, K. et al. Effects of Sr dopant and electric field poling on structural, thermal and dielectric properties of ba<sub>(1-x)</sub>Sr<sub>x</sub>TiO<sub>3</sub> ceramics (x = 0, 0.3, 0.4 and 0.45). *Phase Transii.* **95**, 456–465 (2022).
41. Bharti, C., Sen, A. & Sinha, T. P. Enhanced dielectric and ferroelectric properties of Ca<sup>2+</sup>substituted sodium bismuth titanate. *AIP Conf. Proc.* **1512**, 1306–1307. (2013).
42. He, X. & Mo, Y. Accelerated materials design of Na<sub>0.5</sub>Bi<sub>0.5</sub>TiO<sub>3</sub> oxygen ionic conductors based on first principles calculations. *Phys. Chem. Chem. Phys.* **17**, 18035–18044 (2015).
43. Li, M. et al. A family of oxide ion conductors based on the ferroelectric perovskite Na<sub>0.5</sub>Bi<sub>0.5</sub>TiO<sub>3</sub>. *Nat. Mater.* **13**, 31–35 (2014).
44. Schönleber, M., Klotz, D. & Ivers-Tiffée, E. A method for improving the robustness of linear Kramers-Krönig validity tests. *Electrochim. Acta.* **131**, 20–27. <https://doi.org/10.1016/j.electacta.2014.01.034> (2014).
45. Steinsvik, S., Bugge, R., Gjonnes, J., Taftø, J. & Norby, T. The defect structure of SrTi<sub>1-x</sub>FexO<sub>3-y</sub> (x = 0–0.8) investigated by electrical conductivity measurements and electron energy loss spectroscopy (EELS). *J. Phys. Chem. Solids.* **58**, 969–976. [https://doi.org/10.1016/S0022-3697\(96\)00200-4](https://doi.org/10.1016/S0022-3697(96)00200-4) (1997).
46. Alaka, P. & Govindaraj, R. Complex dielectric and impedance spectroscopic studies in a multiferroic composite of Bi<sub>2</sub>Fe<sub>4</sub>O<sub>9</sub>-BiFeO<sub>3</sub>. *Condens. Matter Phys.* **3**, 44. <https://doi.org/10.3390/condmat3040044> (2018).
47. Gillot, C. & Michenaud, J. P. Electrical conductivity of similarly doped BaTiO<sub>3</sub> single crystal and ceramics in the rhombohedral phase. *Solid State Com.* **90**, 23–25. [https://doi.org/10.1016/0038-1098\(94\)90955-5](https://doi.org/10.1016/0038-1098(94)90955-5) (1994).
48. Chandra Sekhar, K. S. K. R. et al. Structural evolution, dielectric relaxation and modulus spectroscopic studies in Dy substituted NBT-BT ferroelectric ceramics. *J. Mater. Sci.* **32**, 8628–8647. <https://doi.org/10.1007/s10854-021-05506-4> (2021).
49. Almond, D., Duncan, G. K. & West, A. R. The determination of hopping rates and carrier concentrations in ionic conductors by a new analysis of ac conductivity. *Solid State Ionics.* **8**, 159–164. [https://doi.org/10.1016/0167-2738\(83\)90079-6](https://doi.org/10.1016/0167-2738(83)90079-6) (1983).
50. Chen, R. H., Yen, C. C., Shen, C. S. & Fukami, T. Impedance spectroscopy and dielectric analysis in KH<sub>2</sub>PO<sub>4</sub> single crystal. *Solid State Ionics.* **177**, 2857–2864. <https://doi.org/10.1016/j.ssi.2006.05.053> (2006).
51. Macdonald, J. R. Note on the parametrization of the constant-phase admittance element. *Solid State Ionics.* **13**, 147–149 (1984).
52. Hajra, S., Sahoo, S., Das, R. & Choudhary, R. N. P. Structural, dielectric and impedance characteristics of Na<sub>0.5</sub>Bi<sub>0.5</sub>TiO<sub>3</sub>-BaTiO<sub>3</sub> electronic system. *J. Alloys Comp.* **750**, 507–514. <https://doi.org/10.1016/j.jallcom.2018.04.010> (2018).
53. Ang, C., Yu, Z. & Cross, L. E. Oxygen-vacancy-related low-frequency dielectric relaxation and electrical conduction in Bi:SrTiO<sub>3</sub>. *Phys. Rev.* **B62**, 228–236. <https://doi.org/10.1103/PhysRevB.62.228> (2000).
54. Saha, S. & Krupanidhi, S. B. Dielectric response in pulsed laser ablated (Ba, Sr)TiO<sub>3</sub> thin films. *J. Appl. Phys.* **87**, 849–854. <https://doi.org/10.1063/1.371952> (2000).
55. Rani, R., Sharma, S., Rai, R. & Kholkin, A. L. Investigation of dielectric and electrical properties of Mn doped sodium potassium niobate ceramic system using impedance spectroscopy. *J. Appl. Phys.* **110**, 104102. <https://doi.org/10.1063/1.3660267> (2011).
56. Raymond, O., Font, R., Suárez-Almodover, N., Portelles, J. & Siqueiros, M. Frequency-temperature response of ferroelectromagnetic pb(Fe<sub>1/2</sub>Nb<sub>1/2</sub>)O<sub>3</sub> ceramics obtained by different precursors. Part II. Impedance spectroscopy characterization. *J. Appl. Phys.* **97**, 084108. <https://doi.org/10.1063/1.1870100g> (2005).
57. Pradhan, D. K., Choudhary, R. N. P., Rinaldi, C. & Katiyar, R. S. Effect of Mn substitution on electrical and magnetic properties of Bi<sub>0.9</sub>La<sub>0.1</sub>FeO<sub>3</sub>. *J. Appl. Phys.* **106**, 024102. <https://doi.org/10.1063/1.3158121> (2009).
58. Peláiz-Barranco, A., González-Abreu, Y. & López-Noda, R. Dielectric relaxation and conductivity behavior in modified lead titanate ferroelectric ceramics. *J. Phys. Condens. Mater.* **20** (1–10), 505208. (2008).
59. Kang, B. S., Choi, S. K. & Park, C. H. Diffuse dielectric anomaly in perovskite-type ferroelectric oxides in the temperature range of 400–700°C. *J. Appl. Phys.* **94** <https://doi.org/10.1063/1.1589595> (2003). :1904-k 1911.
60. Singh, G., Tiwari, V. & Gupta, P. Role of oxygen vacancies on relaxation and conduction behavior of KNbO<sub>3</sub> ceramic. *J. Appl. Phys.* **107**, 064103. <https://doi.org/10.1063/1.3309745> (2010).
61. Liu, L. et al. Oxygen-vacancy-related high temperature dielectric relaxation and electrical conduction in 0.95K<sub>0.5</sub>Na<sub>0.5</sub>NbO<sub>3</sub>-0.05BaZrO<sub>3</sub> ceramic. *Phys. B Condens. Matter.* **407**, 136–139. <https://doi.org/10.1016/j.jmat.2018.03.001> (2012).
62. Erdem, E. et al. Formation of (Ti<sup>IV</sup>-V<sup>o</sup>) defect dipoles in BaTiO<sub>3</sub> ceramics heat-treated under reduced oxygen partial-pressure. *Funct. Mater. Lett.* **3**, 65–68. <https://doi.org/10.1142/S1793604710000956> (2010).
63. Yang, F. et al. Defect chemistry and electrical properties of sodium bismuth titanate perovskite. *J. Mater. Chem.* **A6**, 5243–5254. <https://doi.org/10.1039/c7ta09245h> (2018).
64. Davson, J. A., Chen, H. & Tanaka, I. Crystal structure, defect chemistry and oxygen ion transport of the ferroelectric perovskite Na<sub>0.5</sub>Bi<sub>0.5</sub>TiO<sub>3</sub>: insights from first-principles calculations. *J. Mater. Chem.* **A3**, 16574–16582 (2015).
65. Dong, S. T. et al. An Ion migration induced self-powered photoelectrical detector based on FAPbBr<sub>3</sub> single crystals. *Cryst. Eng. Comm.* **24**, 2100–2106 (2022).
66. Cox, T. A. *Transition Metal Oxides* Oxford University Press. (1992).
67. Austin, I. G. & Mott, N. F. Polarons in crystalline and non-crystalline materials. *Adv. Phys.* **18**, 41–102. <https://doi.org/10.1080/0018736900101267> (1969).
68. Li, M. et al. Dramatic influence of A-site nonstoichiometry on the electrical conductivity and conduction mechanisms in the perovskite oxide Na<sub>0.5</sub>Bi<sub>0.5</sub>TiO<sub>3</sub>. *Chem. Mater.* **27**, 629–634. <https://doi.org/10.1021/cm504475k> (2015).
69. Fu, Z. et al. Effects of Zr substitution on structure and thermoelectric properties of Bi<sub>2</sub>O<sub>2</sub>Se. *J. Mater. Res. Tech.* **21**, 640–647 (2022).
70. Wang, H. et al. Enhancement of thermoelectric performance by Ag/Bi/Fe co-doping into Cu<sub>3</sub>SbSe<sub>4</sub> ceramics for green thermoelectric applications. *Ceram. Inter.* **50**, 46239–46245 (2024).
71. Suchanicz, J. et al. Effect of electric field poling on structural, thermal, vibrational, dielectric and ferroelectric properties of Na<sub>0.5</sub>Bi<sub>0.5</sub>TiO<sub>3</sub> single crystals. *J. Alloys Comp.* **854**, 157227 (2021).
72. Suchanicz, J. & Kwapulinski, J. X-ray diffraction study of the phase transitions in Na<sub>0.5</sub>Bi<sub>0.5</sub>TiO<sub>3</sub>. *Ferroelectrics* **165**, 249–253. <https://doi.org/10.1080/00150199508228304> (1995).
73. Zvirgzds, J. A., Kapostins, P. P., Zvirgzde, J. V. & Kruzina, T. V. X-ray study of phase transitions in ferroelectric Na<sub>0.5</sub>Bi<sub>0.5</sub>TiO<sub>3</sub>. *Ferroelectrics* **40**, 75–77. <https://doi.org/10.1080/00150198208210600> (1982).

## Acknowledgements

We gratefully acknowledge Polish high-performance computing infrastructure PLGrid (HPC Centers: ACK Cyfronet AGH) for providing computer facilities and support within computational grants no. PLG/2022/015969 and PLG/2023/016854.

### Author contributions

G.Jaęło conceptualization, investigation, writing-original draft preparation, software, validation, K.Kluczewska-Chmielarz visualization, investigation, writing-original draft preparation, validation, J.Suchanicz conceptualization, supervision, A.Kruk review and editing, A. Kania conceptualization, D.Sitko conceptualization, validation, M.Nowakowska-Malczyk formal analysis, M.Łapiński investigation, G.Stachowski review and editing. All authors reviewed the manuscript.

### Declarations

### Competing interests

The authors declare no competing interests.

### Additional information

**Correspondence** and requests for materials should be addressed to G.J. or K.K.-C.

**Reprints and permissions information** is available at [www.nature.com/reprints](http://www.nature.com/reprints).

**Publisher's note** Springer Nature remains neutral with regard to jurisdictional claims in published maps and institutional affiliations.

**Open Access** This article is licensed under a Creative Commons Attribution-NonCommercial-NoDerivatives 4.0 International License, which permits any non-commercial use, sharing, distribution and reproduction in any medium or format, as long as you give appropriate credit to the original author(s) and the source, provide a link to the Creative Commons licence, and indicate if you modified the licensed material. You do not have permission under this licence to share adapted material derived from this article or parts of it. The images or other third party material in this article are included in the article's Creative Commons licence, unless indicated otherwise in a credit line to the material. If material is not included in the article's Creative Commons licence and your intended use is not permitted by statutory regulation or exceeds the permitted use, you will need to obtain permission directly from the copyright holder. To view a copy of this licence, visit <http://creativecommons.org/licenses/by-nc-nd/4.0/>.

© The Author(s) 2025